gels

MDPI

Article

Properties and Interfacial Stabilization of a Crosslinked Hydroxypropyl Guar Aqueous Gel in a CO_2-Rich Mixed-Phase Fracturing Fluid

Guojun Li [1,2], Meilong Fu [1,2,*], Tengfei Chen [2,3,4] and Yuhao Zhu [1,2]

[1] School of Petroleum Engineering, Yangtze University, Wuhan 430100, China; 2023730017@yangtzeu.edu.cn (G.L.); 2024710386@yangtzeu.edu.cn (Y.Z.)
[2] State Key Laboratory of Low Carbon Catalysis and Carbon Dioxide Utilization, Wuhan 430100, China; chentf_cq@petrochina.com.cn
[3] Xi'an Changqing Chemical Group Co., Ltd., Xi'an 710021, China
[4] National Engineering Laboratory for Exploration and Development of Low-Permeability Oil & Gas Fields, Xi'an 710018, China
* Correspondence: 100625@yangtzeu.edu.cn

Abstract

A crosslinked hydroxypropyl guar (HPG) aqueous gel was investigated as the continuous, structure-forming phase of a CO_2-rich mixed-phase fracturing fluid for unconventional gas reservoirs. The CO_2 fraction was first screened by fluid-loss tests, after which the 30%, 40%, and 50% formulations were compared through proppant-settling tests. Although the 30% formulation exhibited the lowest cumulative fluid loss, the 40% formulation showed the lowest proppant-settling velocity and was selected for subsequent evaluation of phase behavior, gel-phase rheology, flow resistance, interfacial stabilization, and true-triaxial fracturing performance. Stable mixed-phase structures were maintained at 20–80 °C and 10–20 MPa, while bubble characteristics, rheology, and pipe-flow resistance showed a distinct response near 40 °C. Comparison with previously reported AM/AA–CO_2 visualization showed that different water-soluble polymers generated different structures after CO_2 mixing. Newly measured surface-tension and viscoelastic data, together with molecular dynamics simulations, indicated that bulk gel rheology alone could not account for this difference. HPG exhibited pronounced enrichment near the CO_2–water interfaces, whereas AM/AA remained predominantly within the aqueous phase. Combined with the component-removal and viscoelasticity results, these findings suggest that HPG-specific interfacial behavior contributes to the formation and organization of dispersed structures, while the crosslinked gel network provides additional bulk viscoelastic support.

Keywords: crosslinked polysaccharide gel; hydroxypropyl guar; CO_2-rich mixed-phase fracturing fluid; gel rheology; interfacial stabilization

Academic Editor: Marieta Constantin

Received: 19 September 2026
Revised: 27 October 2026
Accepted: 2 November 2026
Published: 3 November 2026

Copyright: © 2026 by the authors. Licensee MDPI, Basel, Switzerland. This article is an open access article distributed under the terms and conditions of the Creative Commons Attribution (CC BY) license.

1. Introduction

Unconventional natural gas resources, including shale gas and tight sandstone gas, have become increasingly important components of natural gas supply. Because these reservoirs commonly exhibit ultra-low permeability and complex pore-fracture systems, their commercial development relies heavily on hydraulic fracturing to create conductive fracture networks [1–3]. Conventional water-based fluids, however, require substantial freshwater and may be retained in nano- to microscale pores by capillary forces, ag-

gravating water blocking, clay swelling, particle migration, and permeability impairment [4–6]. Developing low-damage fluids that retain sufficient proppant transport and operational stability is therefore central to efficient and sustainable unconventional gas reservoir stimulation.

CO_2-based fracturing is attractive for unconventional gas reservoirs because CO_2 has low surface tension, high diffusivity, favorable flowback characteristics, and potential compatibility with carbon capture, utilization, and storage [7–9]. Liquid and supercritical CO_2 fracturing have been extensively investigated for reducing water consumption and formation damage [10–13]. CO_2 foams and energized fluids provide alternative approaches for improving fluid transport and operational control [14,15], while near-dry fracturing has also been developed as a low-water stimulation option [16]. Beyond partially replacing water-based fracturing fluids, CO_2-based fracturing offers the potential to integrate reservoir stimulation with geological CO_2 storage, supporting low-carbon oil and gas development. Meng et al. [7] identified adsorption and diffusion as important mechanisms for CO_2 retention in fractured shale reservoirs, while Lin et al. [17] demonstrated that supercritical CO_2 pretreatment could modify shale pore–fracture structures and enhance permeability. Nevertheless, field-oriented studies have identified fluid loss and insufficient proppant transport as major challenges for CO_2 fracturing [18]. These findings highlight the need for CO_2-rich mixed-phase fracturing fluids that balance CO_2 incorporation with fluid-loss control, proppant suspension, and structural stability.

Polymer gels offer one route to addressing this trade-off. Hydroxypropyl guar (HPG), a hydroxypropyl-modified natural polysaccharide, hydrates in water and, after borate crosslinking, forms an aqueous gel network capable of providing viscosity, elasticity, and particulate suspension [19–22]. Advances in crosslinker design and chemical modification have improved the thermal stability and structural robustness of HPG gels [23–25], while studies of friction reduction, fluid-loss control, and proppant transport have expanded their engineering use [26–28]. In this context, HPG should be considered not only as a bulk rheology modifier but also as a functional gel material whose network properties and interfacial behavior may jointly determine the stability of a CO_2-rich mixed phase.

This distinction is important because aqueous polymer systems with measurable viscosity or elasticity do not necessarily form equivalent gel-based mixed-phase structures after contact with CO_2. Published polymer–CO_2 studies have emphasized high-temperature/high-pressure rheology and engineering performance [29,30], whereas recent work on natural polysaccharides indicates that interfacial adsorption and molecular assembly can materially affect the stability of CO_2-containing dispersions [31]. How the borate-crosslinked HPG gel network couples bulk viscoelasticity with polymer adsorption at the CO_2–water interface, and how this coupling governs phase behavior, pipe-flow response, and fracturing performance, remain insufficiently defined.

In this study, a borate-crosslinked HPG aqueous gel was used as the continuous gel phase of a CO_2-rich mixed-phase fracturing fluid for unconventional gas reservoir stimulation. The CO_2 fraction was first screened by fluid-loss tests, and the 30%, 40%, and 50% formulations were then compared by proppant-settling tests. Based on these results, the 40% formulation was selected for subsequent characterization under high-temperature/high-pressure conditions. Mixed-phase structure, gel rheology, and pipe-flow response were evaluated, while surface-tension and viscoelastic measurements, comparison with previously reported AM/AA–CO_2 visualization, and molecular dynamics simulations were combined to clarify the stabilization mechanism. Finally, true-triaxial fracturing was used to assess fracture initiation and propagation. The study establishes a structure–property–function relationship for a functional polysaccharide gel

used in CO_2-rich mixed-phase fracturing.

2. Results and Discussion

2.1. Optimization of CO_2 Fraction in the HPG Gel–CO_2 System

2.1.1. Fluid-Loss Performance

The CO_2 volume fraction is a key compositional parameter affecting the internal structure and engineering performance of the HPG–CO_2 mixed-phase system. An appropriate CO_2 fraction should not only increase CO_2 utilization but also maintain sufficient structural continuity of the polymer-rich phase to support fluid-loss control and proppant-carrying capacity. Therefore, fluid-loss and proppant-settling tests were first conducted to determine a suitable CO_2 fraction for subsequent phase-behavior, rheological, and flow-resistance investigations.

The fluid-loss results are summarized in Table 1 and Figure 1. As the CO_2 volume fraction increased from 10% to 30%, the equivalent cumulative fluid loss after 60 min decreased markedly from 15.87 mL to 1.71 mL. Further increasing the CO_2 volume fraction to 40% resulted in a fluid loss of only 3.12 mL. At a CO_2 volume fraction of 50%, the cumulative fluid loss increased to 12.77 mL, indicating reduced fluid-loss control compared with the 30% and 40% formulations.

Table 1. Fluid-loss parameters of HPG–CO_2 mixed-phase fracturing fluids with different CO_2 volume fractions.

CO_2 Volume Fraction (%)	Fluid Loss at 60 min (mL)	Average Fluid-Loss Rate (mL/min)	Last-10-min Fluid-Loss Rate (mL/min)
10	15.87	0.264	0.268
30	1.71	0.028	0.026
40	3.12	0.052	0.035
50	12.77	0.213	0.067
70	117.19	1.953	1.845

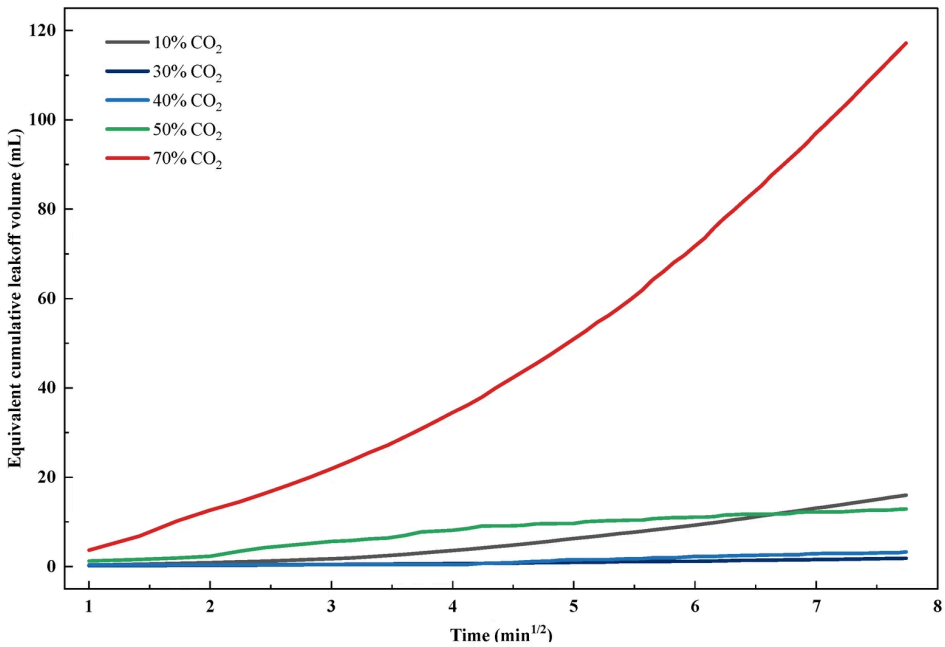


Figure 1. Fluid-loss behavior of HPG–CO_2 mixed-phase fracturing fluids with different CO_2 volume fractions.

In contrast, the 70% CO_2 system exhibited substantially different behavior. The cumulative fluid loss reached 117.19 mL after 60 min, substantially exceeding that of all other tested formulations. This result suggests that excessively high CO_2 contents are unfavorable for fluid-loss control.

Based on the fluid-loss results, the 30%, 40%, and 50% CO_2 volume fractions were selected for further proppant-settling evaluation, while the 10% and 70% CO_2 systems were excluded from subsequent investigation. These results suggest that excessively high CO_2 content may weaken the continuity of the HPG-rich phase and reduce the ability of the mixed-phase system to stabilize the filtration process. Therefore, the fluid-loss behavior provides an initial indication that mixed-phase composition strongly affects the structural integrity of the HPG–CO_2 mixed-phase system.

2.1.2. Proppant-Settling Performance

The proppant-settling velocities of HPG–CO_2 mixed-phase fracturing fluids with different CO_2 volume fractions at various temperatures are presented in Figure 2. Lower settling velocities indicate stronger proppant-carrying and suspension capabilities. By comparing the settling behavior under different temperatures and CO_2 volume fractions, the influence of mixed-phase composition on proppant transport performance can be further evaluated.

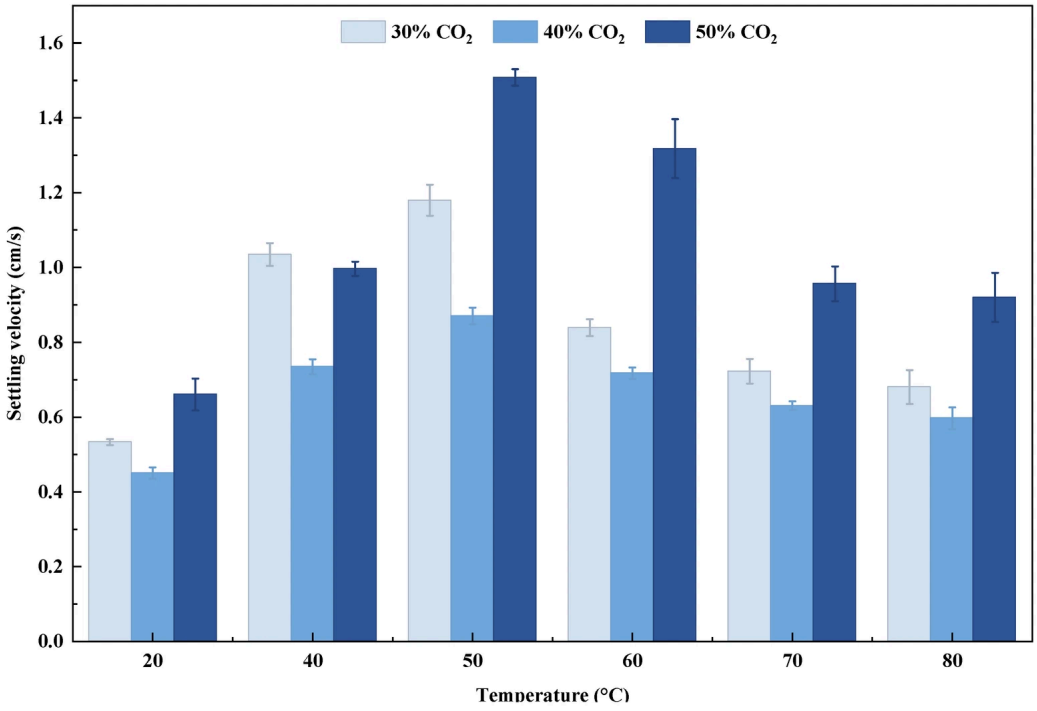


Figure 2. Proppant-settling velocities of HPG–CO_2 mixed-phase fracturing fluids with different CO_2 volume fractions at different temperatures.

Among the investigated systems, the 40% CO_2 mixed-phase fluid consistently exhibited the lowest settling velocity over the entire temperature range, indicating the best proppant-suspension performance. The settling velocity of the 40% CO_2 system remained between 0.45 and 0.87 cm/s, which was lower than those of the 30% and 50% CO_2 systems at all tested temperatures. In contrast, the 50% CO_2 system generally exhibited the highest settling velocities, reaching a maximum value of 1.51 cm/s at 50 °C. These results demonstrate that the CO_2 volume fraction plays a critical role in determining the proppant-carrying capability of the mixed-phase system. An excessively low or

excessively high CO_2 content appears unfavorable for maintaining effective proppant suspension, whereas the intermediate CO_2 volume fraction provides a more balanced mixed-phase structure.

For all three CO_2 volume fractions, the settling velocity exhibited a non-monotonic dependence on temperature, characterized by an initial increase followed by a gradual decrease. At 20 °C, all systems showed relatively low settling velocities. As the temperature increased to 40–50 °C, the settling velocity increased significantly and reached its maximum near 50 °C. It should be noted that the experimental pressure was maintained at 10 MPa, under which CO_2 existed in the liquid state at 20 °C but transitioned to the supercritical state at temperatures above 40 °C. Therefore, the increase in settling velocity from 20 °C to 50 °C may be associated not only with temperature variation but also with changes in the internal structure of the mixed-phase system resulting from the phase transition of CO_2.

Interestingly, further increasing the temperature from 50 °C to 80 °C led to a gradual reduction in settling velocity for all systems. This observation suggests that viscosity reduction caused by temperature increase is not the sole factor governing proppant-settling behavior. Instead, the dispersion characteristics of the mixed-phase fluid may change at elevated temperatures, partially compensating for the adverse effect of viscosity loss and thereby improving the suspension capability. The underlying mechanism will be further discussed in conjunction with the phase-behavior observations and rheological characterization presented in the following sections.

Although the 30% formulation exhibited the lowest cumulative fluid loss, the 40% formulation showed the lowest proppant-settling velocity among the three candidates. Considering both criteria, the 40% CO_2 formulation was selected for subsequent phase-behavior observation, rheological characterization, and flow-resistance evaluation.

2.2. Phase Behavior and Bubble Characteristics of the Gel-Based Mixed Phase

After selecting the 40% CO_2 formulation, visualization experiments were conducted to directly characterize the formation and evolution of the mixed-phase structure under different temperature and pressure conditions. Because the stability of the HPG–CO_2 mixed-phase system depends on the dispersion state of CO_2 within the polymer-rich phase, bubble number and average bubble diameter were quantified using image analysis to describe the structural characteristics of the mixed-phase system.

As shown in Figures 3–6, stable gas–liquid dispersed structures were formed under all tested conditions, and no obvious phase separation was observed. This indicates that the HPG system can not only disperse CO_2 but also maintain a relatively uniform mixed-phase structure, suggesting that HPG participates in stabilizing the gas–liquid dispersed state rather than merely increasing the viscosity of the aqueous phase. However, significant differences in bubble number and bubble-size distribution were observed under different temperature and pressure conditions, suggesting that the microstructure of the system is highly sensitive to thermodynamic conditions.

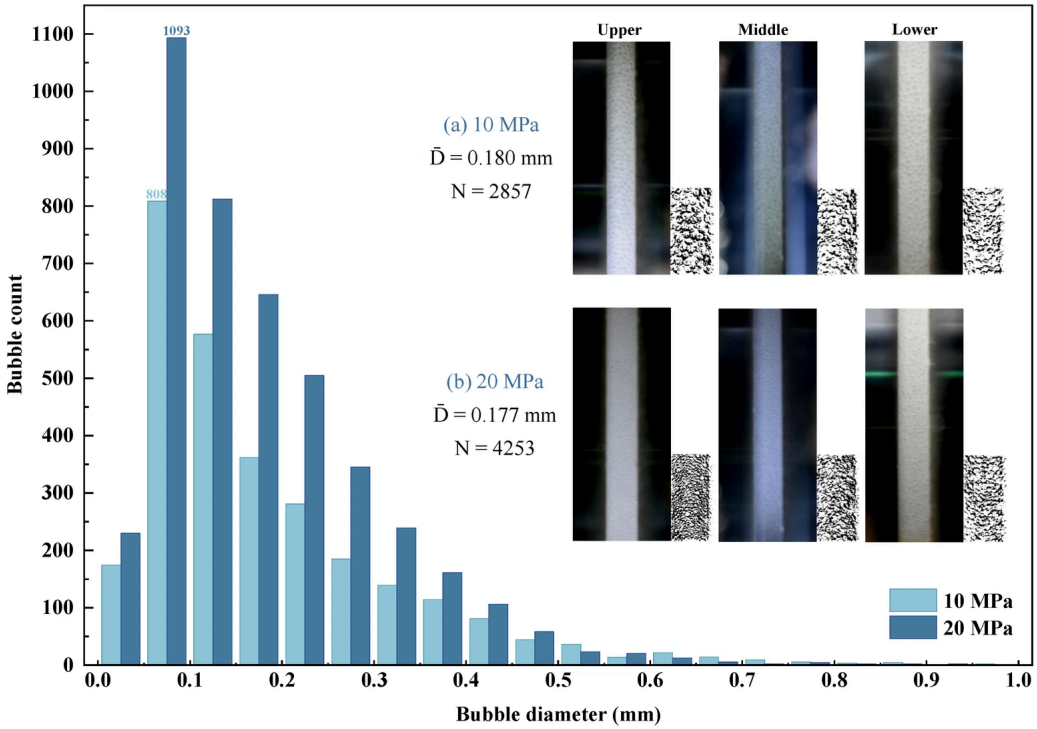


Figure 3. Bubble-size distributions and visualization results at 20 °C.

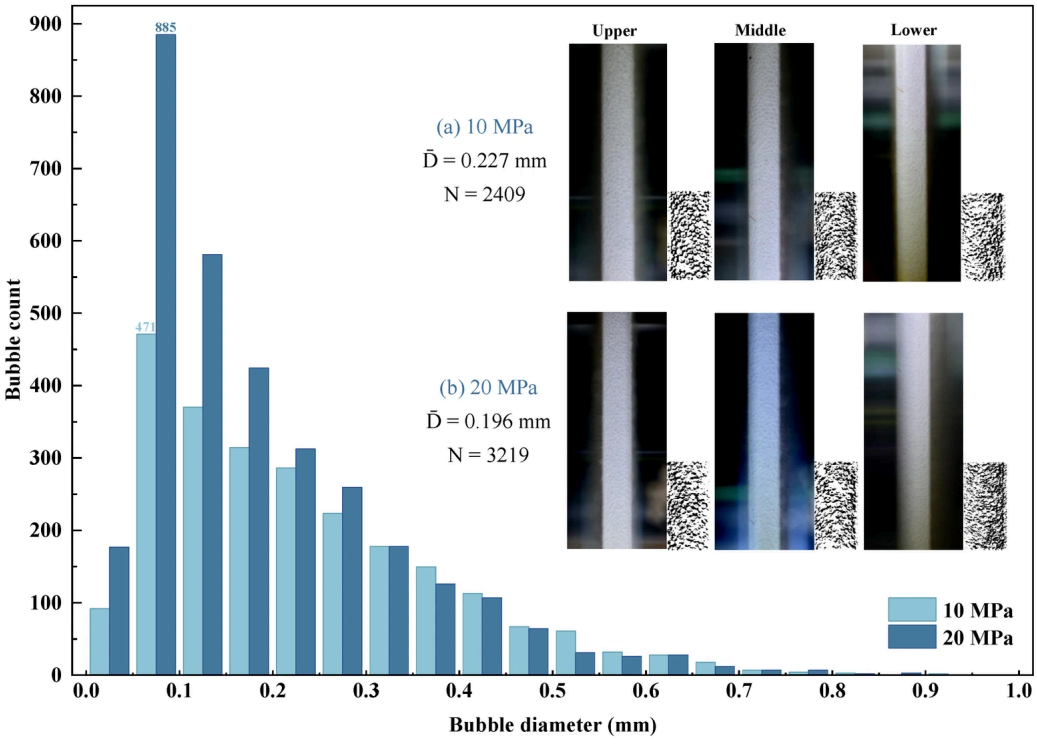


Figure 4. Bubble-size distributions and visualization results at 40 °C.

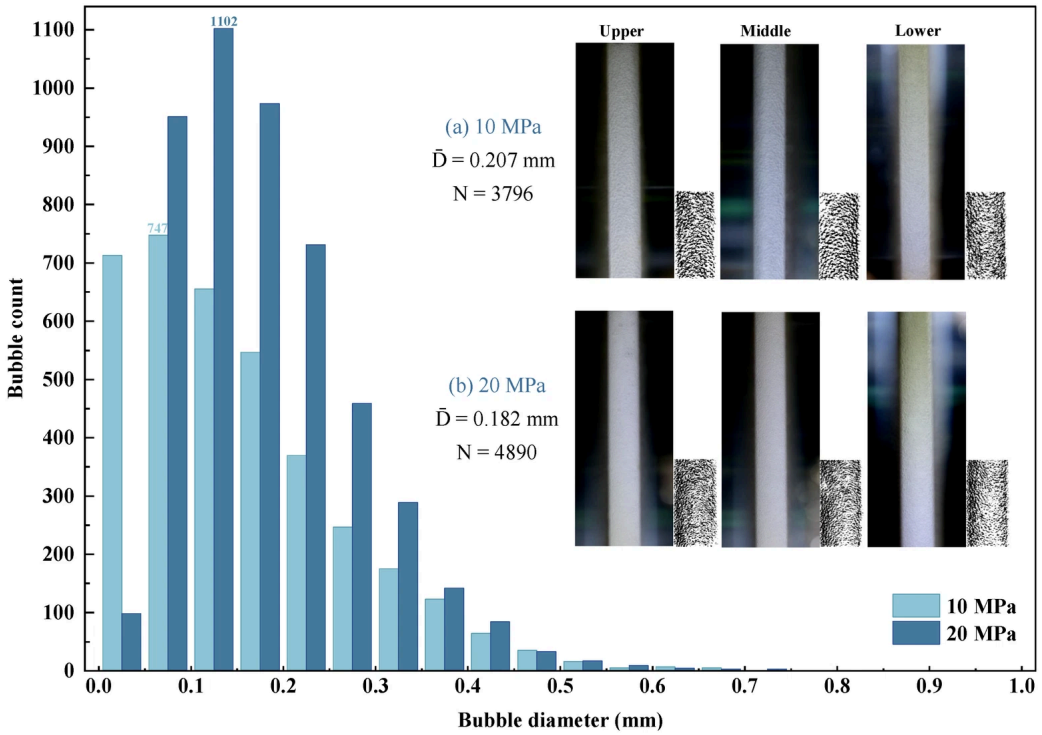


Figure 5. Bubble-size distributions and visualization results at 60 °C.

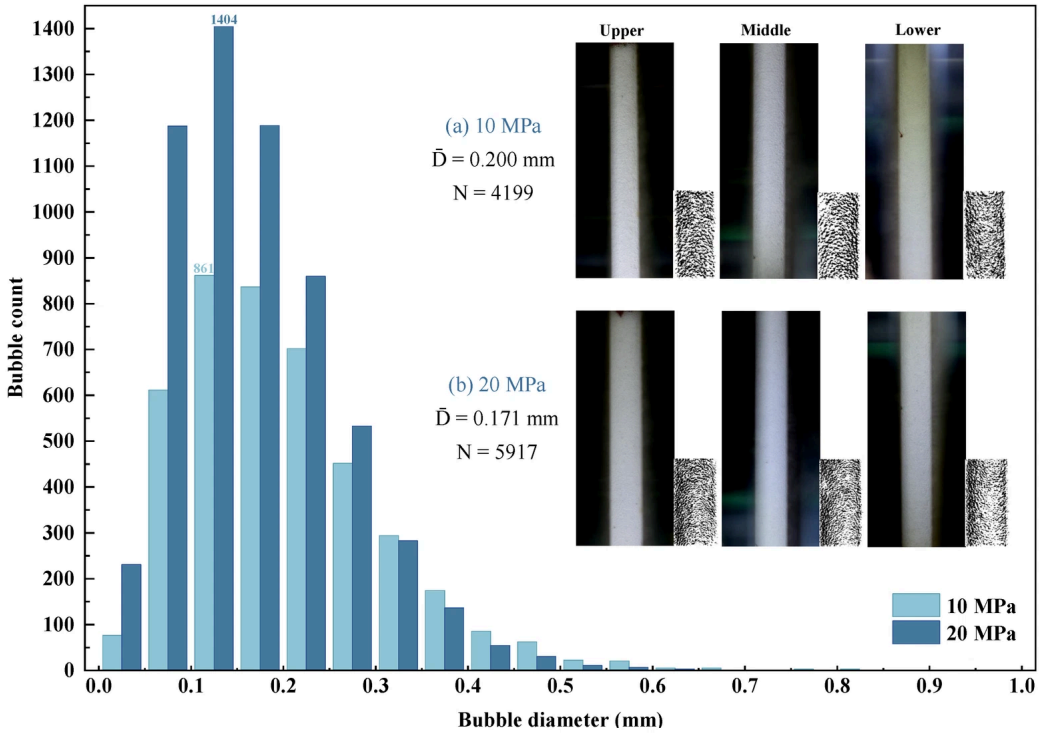


Figure 6. Bubble-size distributions and visualization results at 80 °C.

At a constant temperature, increasing pressure generally increased the total bubble number while reducing the average bubble diameter. For example, at 20 °C, the total bubble number increased from 2857 to 4253 as the pressure increased from 10 to 20 MPa, while the average bubble diameter slightly decreased from 0.180 to 0.177 mm. A similar trend was observed at 80 °C, where the bubble number increased from 4199 to 5917 and the average bubble diameter decreased from 0.200 to 0.171 mm. Overall, higher pres-

sures promoted the formation of a larger number of smaller bubbles, indicating enhanced CO_2 dispersion within the fluid.

In contrast, the influence of temperature exhibited a non-monotonic trend. At 20 °C, the system contained a large number of relatively small bubbles. When the temperature increased to 40 °C, the bubble number decreased noticeably, accompanied by an increase in average bubble diameter. Under 10 MPa, the total bubble number decreased from 2857 to 2409, while the average bubble diameter increased from 0.180 to 0.227 mm. Under 20 MPa, the bubble number decreased from 4253 to 3219 and the average bubble diameter increased from 0.177 to 0.196 mm. As the temperature was further increased to 60 and 80 °C, the bubble number increased again and the average bubble diameter gradually decreased. The highest bubble number, 5917, was obtained at 80 °C and 20 MPa, accompanied by one of the smallest average bubble diameters (0.171 mm). These results indicate that the bubble number and bubble-size distribution changed markedly with temperature, with fewer and larger bubbles observed near 40 °C and more numerous, smaller bubbles observed at higher temperatures.

In addition to the overall statistics, bubble distributions varied slightly along the vertical direction of the visualization cell. The lower region generally contained a larger number of smaller bubbles, whereas the upper region tended to exhibit relatively larger bubble diameters. Nevertheless, the differences among the three regions remained limited, indicating that the mixed-phase system maintained good overall dispersion stability. Detailed bubble-size distributions for the upper, middle, and lower regions under different temperature and pressure conditions are provided in Supplementary Figures S7–S14.

Overall, pressure promotes CO_2 dispersion and bubble refinement, whereas temperature exerts a more complex influence on the microstructure of the mixed-phase system. Notably, the bubble number reached a minimum and the average bubble diameter reached a maximum near 40 °C, indicating a distinct shift in bubble-size distribution within this temperature range. These observations demonstrate that the mixed-phase structure of the HPG–CO_2 system is highly sensitive to temperature and pressure. In particular, the reduced bubble number and increased average bubble diameter near 40 °C indicate a distinct structural transition, which provides an important basis for understanding the rheological and flow-resistance responses discussed in the following sections.

2.3. Rheological Properties of the Crosslinked HPG Gel–CO_2 System

The rheological behavior of the HPG–CO_2 mixed-phase fracturing fluid is influenced by both the HPG network in the aqueous phase and the dispersed CO_2-rich domains within the mixed-phase system. Therefore, steady-shear tests were conducted under different temperature and pressure conditions to evaluate how thermodynamic conditions and mixed-phase structure jointly affect the macroscopic rheological response. The results are presented in Figure 7 and Table 2.

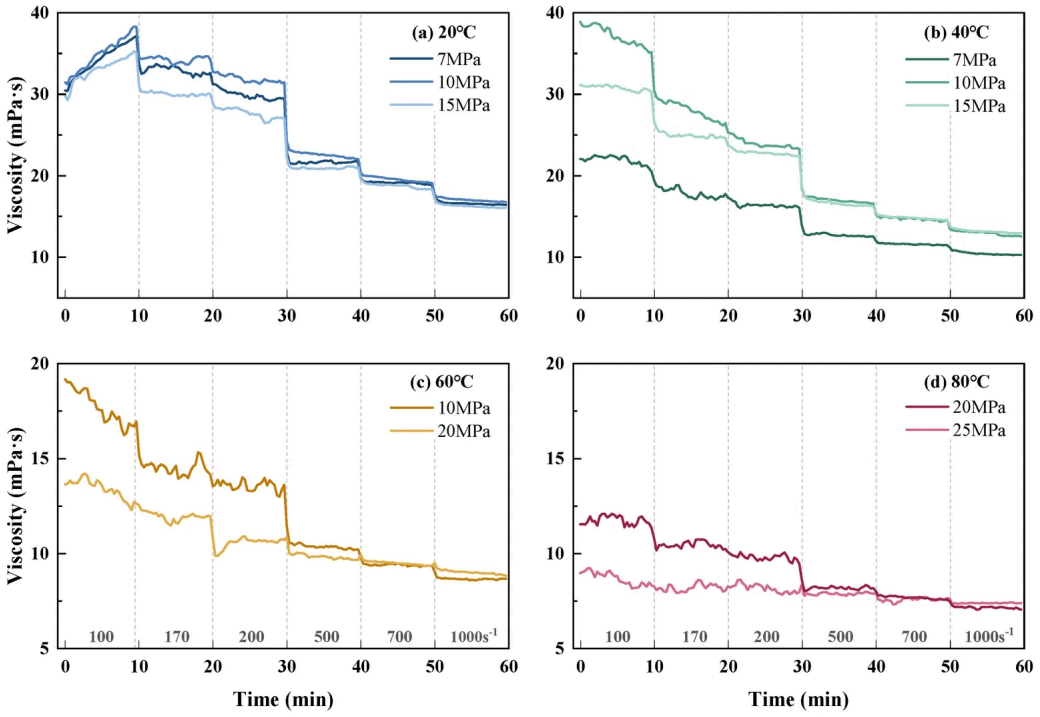


Figure 7. Rheological behavior of HPG–CO_2 mixed-phase fracturing fluid under different temperature and pressure conditions.

Table 2. Apparent viscosity of HPG–CO_2 mixed-phase fracturing fluid under different temperatures, pressures and shear rates.

Temperature (°C)	Pressure (MPa)	Apparent Viscosity Under Different Shear Rates (mPa·s)					
		100 s^{-1}	170 s^{-1}	200 s^{-1}	500 s^{-1}	700 s^{-1}	1000 s^{-1}
20	7	34.20	32.95	29.92	21.66	19.12	16.59
	10	34.89	34.27	31.89	22.59	19.55	17.02
	15	33.13	30.05	27.66	20.96	18.74	16.27
40	7	21.91	17.86	16.37	12.72	11.58	10.44
	10	35.19	28.08	23.94	17.07	14.71	12.93
	15	30.76	24.98	22.81	16.73	14.82	13.16
60	10	17.67	14.49	13.55	10.37	9.38	8.64
	20	13.38	11.94	10.55	9.84	9.48	9.00
80	20	11.72	10.44	9.78	8.17	7.66	7.14
	25	8.66	8.18	8.14	7.87	7.55	7.37

As shown in Figure 7, all tested systems exhibited pronounced shear-thinning behavior, with viscosity continuously decreasing as the shear rate increased from 100 to 1000 s^{-1}. For example, at 20 °C and 10 MPa, the viscosity decreased from 34.89 mPa·s at 100 s^{-1} to 17.02 mPa·s at 1000 s^{-1}, corresponding to a reduction of approximately 51%. This behavior indicates that the HPG–CO_2 mixed-phase fluid possesses typical non-Newtonian characteristics, and that its internal structure can undergo orientation and rearrangement under increasing shear conditions, resulting in a lower apparent viscosity. Such shear-thinning behavior can be attributed to the orientation and rearrangement of the HPG network, together with shear-induced deformation of the dispersed mixed-phase structure. Even at a high shear rate of 1000 s^{-1}, the viscosity remained within the range of 7.14–17.02 mPa·s, indicating that the fluid retained a certain degree of structural

integrity under high-shear conditions without experiencing complete viscosity loss.

Temperature exerted a significant influence on the rheological properties of the system. In general, viscosity decreased with increasing temperature. At a shear rate of 100 s^{-1}, the viscosity at 20 °C and 10 MPa was 34.89 mPa·s, which decreased to 17.67 and 11.72 mPa·s at 60 and 80 °C, respectively. Similar trends were observed at other shear rates, indicating that elevated temperatures weakened the internal interactions within the system and consequently reduced its apparent viscosity.

However, the rheological response exhibited distinctive behavior at 40 °C. At this temperature, the viscosities measured at 10 and 15 MPa remained relatively high. For instance, at 100 s^{-1}, viscosities of 35.19 and 30.76 mPa·s were obtained at 10 and 15 MPa, respectively, which were comparable to those measured at 20 °C. In contrast, the viscosity at 7 MPa decreased markedly to 21.91 mPa·s. These results indicate that the rheological behavior of the system becomes considerably more sensitive to pressure near 40 °C, suggesting an enhanced response of fluid properties to pressure variations within this temperature range.

When combined with the visualization results shown in Figures 3–6, it can be observed that the total bubble number reached a minimum while the average bubble diameter reached a relatively high value at 40 °C. Although the current dataset does not allow the specific contributions of different factors to the observed performance variations to be fully distinguished, both the visualization and rheological results consistently indicate that 40 °C represents a temperature range in which the macroscopic response of the system is particularly sensitive.

Pressure generally contributed to maintaining a higher viscosity, although its influence gradually weakened as temperature increased. At 20 and 40 °C, noticeable viscosity differences were observed among different pressure conditions. In contrast, the viscosity gap became much smaller at 60 and 80 °C. For example, at 1000 s^{-1}, the viscosities at 60 °C were 8.64 and 9.00 mPa·s under 10 and 20 MPa, respectively, whereas the corresponding values at 80 °C were 7.14 and 7.37 mPa·s under 20 and 25 MPa. These results suggest that temperature gradually becomes the dominant factor governing the rheological behavior of the system at elevated temperatures, while the influence of pressure becomes less pronounced.

Overall, the HPG–CO_2 mixed-phase fracturing fluid exhibited favorable shear-thinning characteristics and stable rheological performance over a wide range of temperatures and pressures. Although viscosity generally decreased with increasing temperature, the system displayed a distinctive response near 40 °C that differed from those observed at other temperatures. Combined with the visualization results, this temperature range appears to exhibit enhanced sensitivity to temperature and pressure variations, suggesting that it may represent an important window for performance evolution within the mixed-phase system. These results indicate that the rheological behavior of the HPG–CO_2 mixed-phase fracturing fluid is structure-dependent, and the influence of this structural response on flow resistance will be further examined in the following section.

2.4. Flow Resistance Characteristics

To further determine whether the structural and rheological responses described above are reflected in dynamic flow, pressure-drop and friction-factor measurements were conducted at various flow velocities and temperatures. The pressure-drop behavior is shown in Figure 8, while the corresponding friction factors are presented in Figure 9. Friction factor contour maps are provided as embedded figures to facilitate comparison of the overall variation trends.

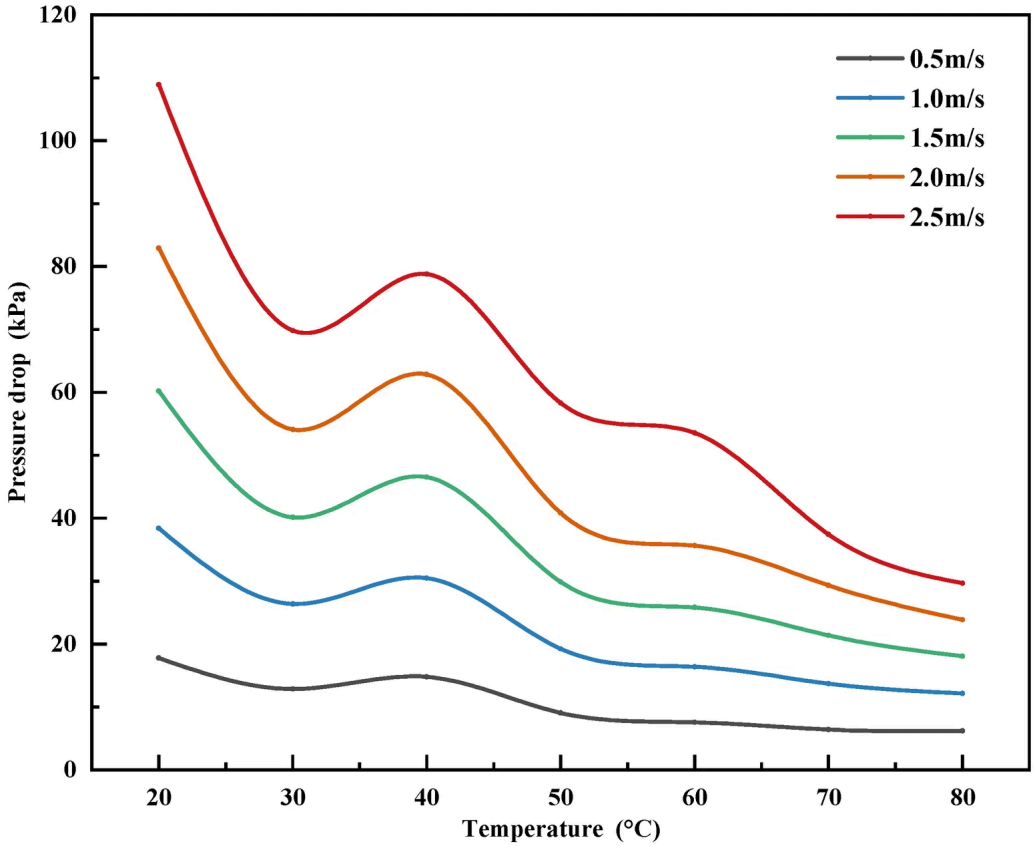


Figure 8. Pressure-drop behavior of HPG–CO_2 mixed-phase fracturing fluid at different temperatures and flow velocities.

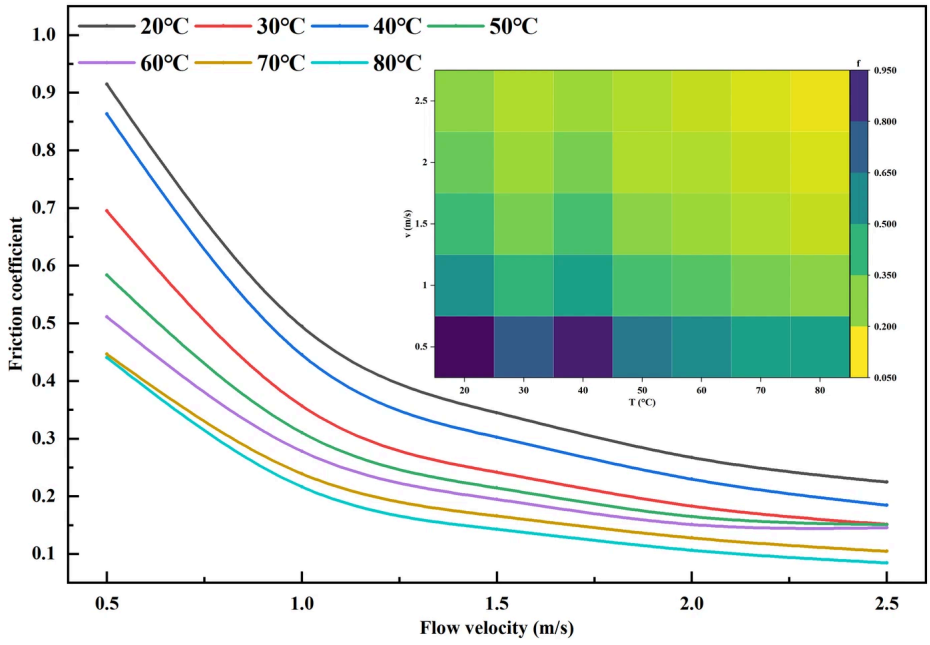


Figure 9. Friction factors of HPG–CO_2 mixed-phase fracturing fluid under different temperature and flow conditions.

As shown in Figure 8, the pressure drop generally decreased with increasing temperature under all tested flow conditions. Taking the flow velocity of 2.5 m/s as an example, the pressure drop decreased from 108.90 kPa at 20 °C to 69.82 kPa at 30 °C, increased to 78.82 kPa at 40 °C, and then continuously decreased to 29.63 kPa at 80 °C. Similar trends were observed at other flow velocities, where a local increase in pressure drop occurred within the temperature range of 30–40 °C. These results indicate that although increasing temperature generally reduces flow resistance, a distinct deviation from the overall trend occurs near 40 °C.

The variation in friction factor with flow velocity is presented in Figure 9. Under a given temperature condition, the friction factor decreased continuously with increasing flow velocity. For example, at 20 °C, the friction factor decreased from 0.915 at 0.5 m/s to 0.225 at 2.5 m/s, while at 80 °C it decreased from 0.441 to 0.085. This behavior indicates that the additional resistance associated with unit flow velocity gradually decreases as flow velocity increases, reflecting the non-linear flow characteristics of the mixed-phase system.

The friction factor contour maps further demonstrate the influence of temperature on flow resistance. In general, higher-temperature regions corresponded to lower friction factors, whereas lower-temperature regions exhibited relatively higher resistance. However, consistent with the pressure-drop results, a distinct local maximum appeared at 40 °C. This phenomenon was particularly evident at low flow velocities. For example, at 0.5 m/s, the friction factor increased from 0.695 at 30 °C to 0.863 at 40 °C before decreasing to 0.584 at 50 °C. These results indicate that the anomalous response near 40 °C is reflected not only in the pressure-drop behavior but also in the overall flow-resistance characteristics of the system.

When the friction results are compared with the visualization and rheological results, a consistent trend can be identified near 40 °C. The visualization experiments showed that the total bubble number reached a minimum while the average bubble diameter increased to a relatively high level. The rheological experiments revealed enhanced pressure sensitivity in this temperature range, whereas the friction experiments exhibited locally elevated pressure drops and friction factors. Collectively, these observations indicate that 40 °C does not represent an ordinary point along the continuous evolution of system properties, but rather corresponds to a temperature range in which the mixed-phase structure, rheological response, and flow resistance characteristics change simultaneously.

To further understand the anomalous response observed near 40 °C, the possible influencing factors were analyzed. From the perspective of temperature-dependent behavior, the performance evolution within the range of 20–40 °C may be closely related to the rapid variation in CO_2 thermophysical properties. As the temperature increased from 20 to 40 °C, the system transitioned from liquid-CO_2 conditions to supercritical-CO_2 conditions, accompanied by reduced CO_2 density, enhanced diffusivity, and a decrease in continuous-phase viscosity. For gas–liquid dispersed systems, the reduction in continuous-phase viscosity may weaken liquid-film stability, whereas the enhanced diffusivity of CO_2 may promote gas transfer between bubbles and facilitate bubble growth. Consequently, the reduction in bubble number and the increase in average bubble diameter observed near 40 °C may be related to these thermophysical-property variations. Meanwhile, the rheological results indicate that the apparent viscosity did not decrease substantially with increasing temperature, suggesting that changes in bubble structure may partially offset the viscosity reduction caused by temperature elevation, thereby maintaining a relatively high apparent viscosity. Further considering the friction results, both the pressure drop and friction factor at 40 °C remained higher than those at adja-

cent temperatures, indicating that flow resistance did not decrease synchronously with viscosity. Therefore, the local increase in frictional resistance near 40 °C may be associated with the combined effects of CO_2 thermophysical-property variation and the corresponding changes in dispersion characteristics, rather than being controlled solely by the viscosity of the continuous phase.

As the temperature further increased to 60–80 °C, the bubble number increased again and the average bubble diameter decreased, indicating an improvement in gas–liquid dispersion. However, the apparent viscosity, pressure drop, and friction factor all continued to decrease with increasing temperature. These observations suggest that, under high-temperature conditions, the reduction in continuous-phase viscosity and the gradual weakening of the polymer network become increasingly important factors governing flow behavior, whereas the contribution of bubble-size variation to the overall flow behavior may become less pronounced. Therefore, the HPG–CO_2 mixed-phase fracturing fluid exhibits different controlling characteristics in different temperature ranges. The range of 20–40 °C is primarily characterized by anomalous responses associated with rapid CO_2 thermophysical-property variation, whereas in the range of 60–80 °C, the influence of continuous-phase rheological properties gradually becomes dominant. These results further confirm that the macroscopic flow performance of the HPG–CO_2 mixed-phase fracturing fluid is closely related to the evolution of its mixed-phase structure. Therefore, understanding the formation and stabilization mechanism of this structure is necessary for explaining the overall performance of the system.

2.5. Gel-Network-Mediated Formation and Stabilization Mechanism

The results presented above demonstrate that the borate-crosslinked HPG aqueous gel can act as a continuous, structure-forming phase for stable gas–liquid dispersed structures over a wide range of temperature and pressure conditions. Its favorable rheology, flow performance, and proppant-carrying capacity reflect the contribution of the HPG gel network to bulk structure. However, these macroscopic gel properties alone do not fully explain why the mixed-phase structure forms and remains stable.

To distinguish the contribution of gel-phase surface tension and bulk viscoelasticity from polymer-specific interfacial organization, an AM/AA copolymer solution was introduced as a comparison system. The AM/AA copolymer is a water-soluble synthetic polymer with measurable viscoelasticity and has been investigated previously in CO_2–water polymer hybrid fracturing fluids under high-temperature and high-pressure conditions. Under comparable experimental conditions, the AM/AA system generally exhibited a milky appearance after CO_2 mixing, in contrast to the more clearly distinguishable bubble-rich structures observed in the HPG system. This difference highlights the distinct dispersed-phase characteristics of the two polymer systems. Representative images of the AM/AA copolymer–CO_2 system reported by Chen et al. [29] are provided in Supplementary Figure S15 for comparison.

This contrast shows that measurable bulk viscoelasticity does not by itself guarantee formation of a stable gel-based mixed phase. The AM/AA system was therefore used not as a competing formulation but as a comparison for identifying the roles of the crosslinked HPG gel network and HPG-specific interfacial adsorption. Component-removal experiments were first conducted to evaluate the contribution of each component to the HPG gel formulation. Surface-tension measurements and dynamic viscoelastic characterization were then used to test whether interfacial activity or bulk gel rheology could explain the observed difference. Finally, molecular dynamics simulations compared the interfacial migration, adsorption behavior, and conformational evolution of HPG and AM/AA copolymer molecules at the CO_2–water interface.

2.5.1. Experimental Verification

Component-removal visualization tests were conducted at 40 °C and 10 MPa to distinguish the contributions of NaOH and crosslinker to the formation of the HPG–CO_2 dispersed structure. As shown in Supplementary Figures S16–S18, visible gas–liquid dispersed structures were observed in the HPG–CO_2 system without either additive, as well as in systems containing NaOH or crosslinker. Under the tested conditions, therefore, neither NaOH nor crosslinker was indispensable for producing visible dispersed structures. The differences among the tested formulations were mainly reflected in bubble appearance and spatial distribution, suggesting that these additives modify the structural characteristics of the HPG–CO_2 system rather than being solely responsible for its ability to generate dispersed structures. However, these visualization tests do not quantify the individual contributions of the additives to the longer-term stability of the complete crosslinked gel.

To examine whether differences in surface activity could explain the contrasting mixed-phase behaviors, surface-tension measurements were performed, and the results are summarized in Table 3. The measured surface tensions of the HPG, HPG + NaOH, and AM/AA copolymer systems were 39.82 ± 2.75, 45.07 ± 0.56, and 42.46 ± 0.34 mN/m, respectively. Although the values were not identical, they fell within a relatively narrow range of approximately 40–45 mN/m. Thus, the measured surface-tension differences alone do not adequately explain the distinct morphologies observed for the HPG-based and AM/AA systems. The AM/AA visualization images used for qualitative comparison were previously reported by Chen et al. [29] and were not newly acquired in the present study (Supplementary Figure S15).

Table 3. Surface-tension and rheological properties of the HPG and AM/AA comparison fluids measured in the present study.

System	Surface Tension (mN/m)	G′ (Pa, 1 Hz)	G″ (Pa, 1 Hz)	G′/G″
HPG	39.82 ± 2.75	0.348	0.790	0.44
HPG + NaOH	45.07 ± 0.56	0.206	0.582	0.35
HPG + Crosslinker	—	3.980	0.745	5.34
HPG + Crosslinker + NaOH	—	5.251	0.939	5.59
AM/AA copolymer	42.46 ± 0.34	2.433	2.051	1.19

Note: "—" indicates that surface tension was not reported for the crosslinked gel systems.

In addition to surface activity, bulk viscoelasticity was examined as a possible contributor to dispersed-structure formation. As summarized in Table 3, the addition of crosslinker increased the storage modulus (G′) from 0.348 Pa for HPG to 3.980 Pa for HPG + crosslinker and 5.251 Pa for HPG + crosslinker + NaOH. The corresponding G′/G″ ratios increased from 0.44 to 5.34 and 5.59, respectively. In contrast, the addition of NaOH alone did not enhance the elastic response, with G′ and G′/G″ decreasing to 0.206 Pa and 0.35, respectively. The AM/AA copolymer exhibited a G′ of 2.433 Pa and a G′/G″ ratio of 1.19, both higher than those of the un-crosslinked HPG solution. Nevertheless, visible dispersed structures were observed in the un-crosslinked HPG–CO_2 system. This comparison suggests that a high bulk elastic modulus is not a prerequisite for the formation of visible dispersed structures and that bulk viscoelasticity alone cannot fully explain the distinct mixed-phase behaviors of the HPG and AM/AA systems. Crosslinking, however, substantially enhances the bulk elastic response of the complete HPG formulation and may contribute to its structural integrity.

Taken together, the component-removal experiments demonstrate that neither NaOH nor crosslinker is individually necessary for the formation of visible dispersed structures under the tested conditions. The surface-tension and viscoelasticity results further indicate that neither measured surface activity nor bulk rheological properties alone can fully account for the observed differences between the HPG and AM/AA systems. These findings motivated molecular dynamics simulations to compare the interfacial migration, accumulation, and conformational evolution of HPG and AM/AA copolymer chains at the CO_2–water interface.

2.5.2. Molecular Simulation Analysis

To further elucidate the microscopic mechanism responsible for the formation of the HPG–CO_2 mixed-phase structure, a CO_2–water–polymer interfacial model was established, and molecular dynamics simulations were performed for both HPG and AM/AA copolymer systems over 100 ns. Initially, polymer molecules were uniformly distributed within the aqueous phase, and structural evolution was subsequently carried out under NPT conditions. The structural evolution of the two polymer systems was examined using root mean square deviation (RMSD), as shown in Supplementary Figure S19. In both systems, the RMSD increased rapidly during the initial stage and gradually approached a plateau at later simulation times, indicating that the conformational changes became less pronounced as the simulations progressed. This behavior provided a basis for examining the subsequent time-dependent density distributions, interaction energies, and polymer conformations.

(1) Density distribution analysis

Figure 10 presents the z-axis number-density distributions of HPG and AM/AA copolymer at 0, 10, 50, and 100 ns. Initially, both polymers were primarily distributed within the aqueous phase. As the simulation progressed, the HPG density progressively shifted toward the two CO_2–water interfaces, with pronounced density peaks developing in both interfacial regions by 100 ns. Meanwhile, the polymer density in the central aqueous region decreased substantially, indicating the redistribution of HPG chains from the bulk water phase toward the interfaces.

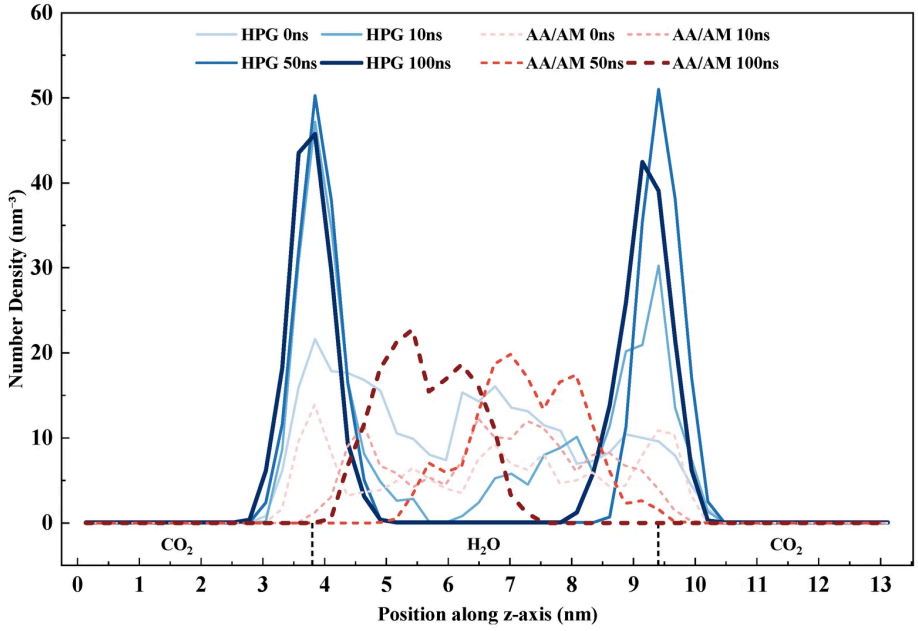


Figure 10. Density distribution evolution of HPG and AM/AA copolymer at the CO_2–water interface.

In contrast, the AM/AA copolymer remained predominantly distributed within the aqueous phase throughout the simulation. Its density peaks were consistently located in the central water region, with no comparable enrichment near the CO_2–water interfaces. The time-resolved density profiles in Supplementary Figures S20–S21 further illustrate these contrasting behaviors: HPG progressively accumulated near the interfaces, whereas AM/AA largely retained its distribution within the aqueous phase.

These results reveal distinct interfacial distribution behaviors between HPG and AM/AA copolymer. Combined with the visualization results in Section 2.5.1, the pronounced interfacial enrichment of HPG suggests that the intrinsic interfacial behavior of the polymer chains contributes to the formation of the HPG–CO_2 dispersed structure.

(2) Interaction energy analysis

To further examine the molecular interactions associated with the distinct interfacial distribution behaviors, the interaction energies between the polymer chains and the surrounding CO_2 and water molecules were analyzed, as shown in Figure 11. The figure presents the time evolution of the Coulombic and Lennard-Jones (LJ) interaction-energy components. At the end of the simulation, the reported total interaction energy between HPG and CO_2 was approximately -3.8×10^3 kJ·mol^{-1}, while that between HPG and water was approximately -1.45×10^4 kJ·mol^{-1}. For the AM/AA copolymer system, the corresponding values were approximately -3.0×10^3 kJ·mol^{-1} for AM/AA–CO_2 and -2.5×10^4 kJ·mol^{-1} for AM/AA–water.

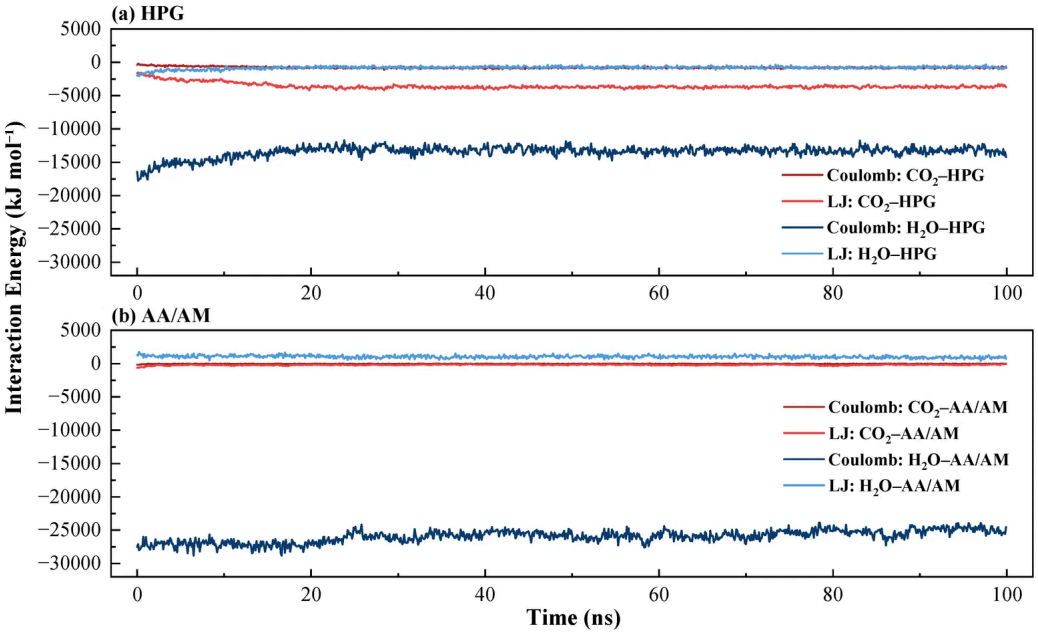


Figure 11. Interaction energies between polymers and surrounding fluid phases during simulation.

In both systems, the polymer–water interaction energy exhibited a greater negative magnitude than the corresponding polymer–CO_2 interaction energy, indicating substantial interactions between the polymer chains and the aqueous phase under the simulated conditions. However, the two polymers exhibited markedly different spatial distributions despite this general feature. As shown in Figure 10, HPG progressively accumulated near the CO_2–water interfaces, whereas AM/AA remained predominantly distributed within the aqueous phase. These results indicate that the interaction-energy profiles alone do not fully explain the contrasting interfacial distribution behaviors observed for the two polymers. To further investigate the structural differences associated with these

behaviors, the evolution of polymer-chain conformation was examined using the radius of gyration (Rg) and solvent-accessible surface area (SASA).

(3) Polymer conformational evolution analysis

The conformational evolution of the polymer chains was further examined using the radius of gyration (Rg) and solvent-accessible surface area (SASA), as shown in Figure 12. The Rg of HPG fluctuated within a relatively narrow range of approximately 0.9–1.0 nm throughout the simulation. In comparison, the Rg of the AM/AA copolymer exhibited a slight downward trend, decreasing from approximately 0.85 nm to around 0.8 nm. A similar difference was observed in the SASA profiles. The SASA of HPG remained relatively stable, fluctuating mainly between 190 and 205 nm^2, whereas that of the AM/AA copolymer gradually decreased from approximately 150 nm^2 to 120 nm^2 over the simulation period.

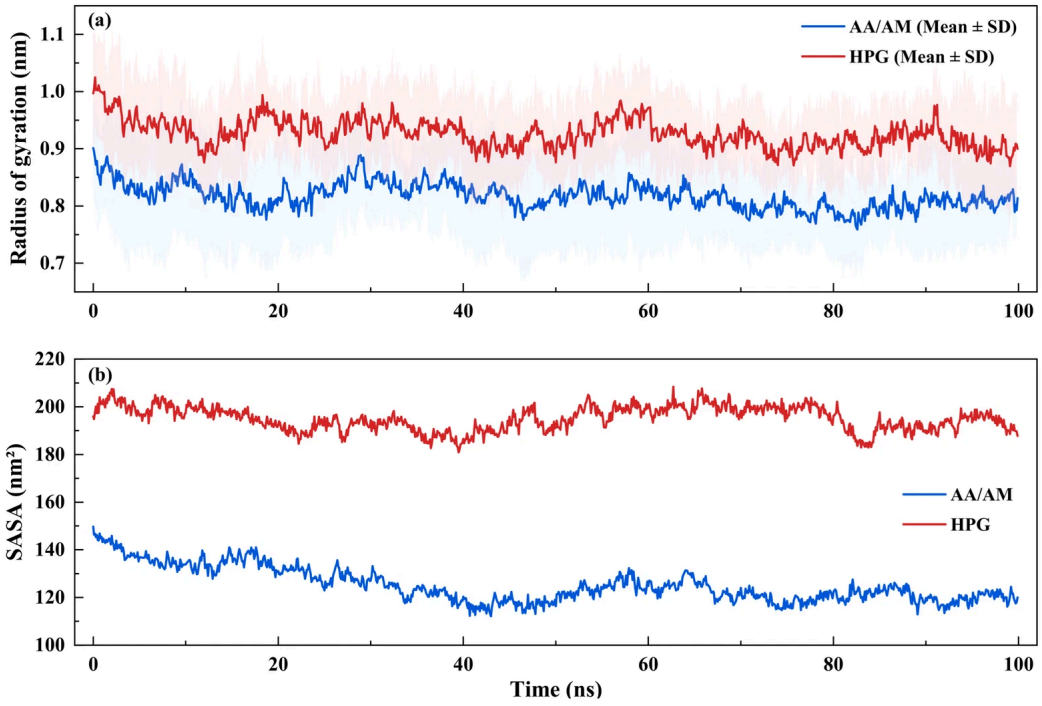


Figure 12. Evolution of radius of gyration (Rg) and solvent-accessible surface area (SASA) of polymer chains.

The radius of gyration characterizes the spatial distribution of a polymer chain around its center of mass, while SASA quantifies the surface area accessible to the surrounding medium. The relatively stable Rg and SASA profiles of HPG indicate that its conformational characteristics and solvent-accessible surface were largely maintained during the simulation. In contrast, the concurrent decreases in Rg and SASA for AM/AA suggest gradual chain contraction accompanied by a reduction in its solvent-accessible surface area. These contrasting conformational trends complement the density distribution results in Figure 10, providing additional insight into the different structural evolution of the two polymer systems. The corresponding molecular configurations are further illustrated in Figure 13 and Supplementary Figures S22–S23.

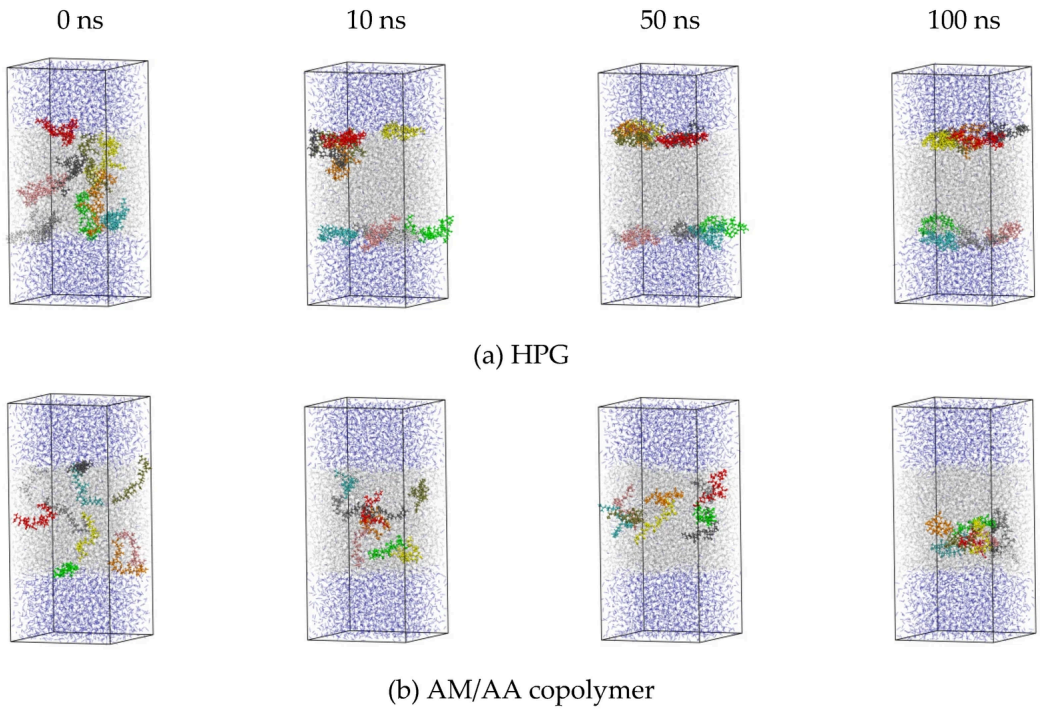


Figure 13. Representative molecular configuration snapshots of HPG and AM/AA copolymer during simulation.

(4) Molecular configuration snapshot analysis

To visualize the spatial evolution of the polymer chains, representative molecular configuration snapshots of HPG and AM/AA copolymer at 0, 10, 50, and 100 ns are presented in Figure 13, while the complete evolution processes are provided in Supplementary Figures S22–S23. As shown in Figure 13, HPG chains were initially distributed within the aqueous phase and progressively redistributed toward the two CO_2–water interfacial regions as the simulation proceeded. At 50 and 100 ns, HPG chains were visibly concentrated near the interfaces, consistent with the pronounced interfacial density peaks observed in Figure 10.

In contrast, the AM/AA copolymer remained predominantly distributed within the central aqueous phase throughout the simulation, without comparable accumulation near the CO_2–water interfaces. The snapshots therefore provide a visual counterpart to the density distribution analysis, illustrating the distinct spatial evolution of the two polymer systems. Together with the conformational evolution shown in Figure 12, these observations reveal contrasting interfacial distribution and chain-configuration behaviors between HPG and AM/AA copolymer under the simulated conditions.

(5) Formation mechanism discussion

Taken together, the experimental observations and molecular simulation results suggest that the formation and structural maintenance of the HPG–CO_2 mixed-phase system involve complementary contributions from polymer-specific interfacial behavior and the bulk viscoelasticity of the gel network. Neither surface tension nor macroscopic viscoelasticity alone adequately explains the contrasting mixed-phase behaviors observed for the HPG and AM/AA systems.

The component-removal experiments showed that visible gas–liquid dispersed structures could still form when alkali or crosslinker was omitted, although the bubble size and distribution characteristics changed. This indicates that these additives modify the characteristics of the dispersed structures, whereas the presence of HPG itself is

closely associated with their formation. The surface-tension measurements further showed that the HPG, HPG + NaOH, and AM/AA systems had values within a relatively narrow range of approximately 40 mN/m. Meanwhile, the AM/AA system exhibited a measurable elastic response, with a storage modulus (G′) of 2.433 Pa and a G′/G″ ratio of 1.19, whereas the fully formulated HPG system exhibited a substantially higher G′ of 5.251 Pa and a G′/G″ ratio of 5.59. These results indicate that differences in surface tension and the mere presence of bulk elasticity are insufficient to account for the distinct mixed-phase behaviors. Instead, the molecular characteristics of the polymer and the resulting interfacial organization warrant further consideration.

The molecular simulation results provide insight into this difference. Density distributions and molecular configuration snapshots showed that HPG chains progressively accumulated near the CO_2–water interfaces, whereas AM/AA copolymer chains remained predominantly within the aqueous phase. In addition, the Rg and SASA of HPG remained relatively stable during the simulation, while both parameters decreased for AM/AA. Together, these observations indicate that HPG exhibited a distinct tendency toward interfacial accumulation while maintaining its conformational characteristics under the simulated conditions. Such interfacial enrichment may facilitate polymer coverage of newly generated gas–liquid interfaces and thereby contribute to the formation and organization of the dispersed structure. The interaction-energy profiles provide complementary information on polymer–fluid interactions, but do not independently establish a quantitative ranking of the intrinsic interfacial affinities of the two polymers. The contrasting spatial distributions and conformational evolution therefore provide the more direct molecular-level evidence for interpreting their different behaviors.

The respective roles of polymer interfacial behavior and gel-network rheology can consequently be distinguished. The component-removal experiments indicate that crosslinking is not a prerequisite for the formation of visible gas–liquid dispersed structures. However, the marked increase in G′ following the addition of crosslinker and alkali demonstrates that formulation components substantially enhance the bulk elastic response of the HPG system. The results therefore support a complementary mechanism in which the interfacial behavior of HPG chains contributes to the formation and organization of the dispersed structure, while the crosslinked gel network provides additional bulk elastic support that may help maintain the structure during deformation and flow. This interpretation links the molecular-scale interfacial behavior to the macroscopic rheological and flow characteristics of the HPG–CO_2 mixed-phase fracturing fluid without attributing all aspects of its performance to a single mechanism.

The molecular simulations were conducted using simplified polymer-chain models, with a degree of polymerization of 4 for HPG and 8 for AM/AA, rather than an explicit representation of the high-molecular-weight, borate-crosslinked HPG network. Accordingly, the simulations are used to compare the interfacial behavior and conformational evolution of the two polymer types, rather than to reproduce the complete structure or quantitatively establish the long-term stability of the actual crosslinked gel. Differences in model size and composition also mean that absolute interaction energies and conformational parameters should not be interpreted as direct, normalized measures of intrinsic interfacial affinity or coverage capacity. Moreover, the present results do not directly quantify bubble-coalescence kinetics or isolate the contribution of crosslinking to long-term dispersion stability. Within these boundaries, the combined experimental and simulation evidence supports a mechanistic interpretation in which HPG-specific interfacial behavior contributes to mixed-phase formation, while the crosslinked gel network provides additional bulk structural support. This coupled perspective helps explain why the HPG and AM/AA systems exhibit different mixed-phase

behaviors despite their broadly comparable measured surface-tension levels and their respective viscoelastic responses.

2.6. True-Triaxial Fracturing Verification

To evaluate the fracturing capability of the selected 40% CO_2 HPG–CO_2 mixed-phase fracturing fluid, true-triaxial fracturing experiments were conducted. The injection-pressure response and the post-fracturing specimen are shown in Figure 14.

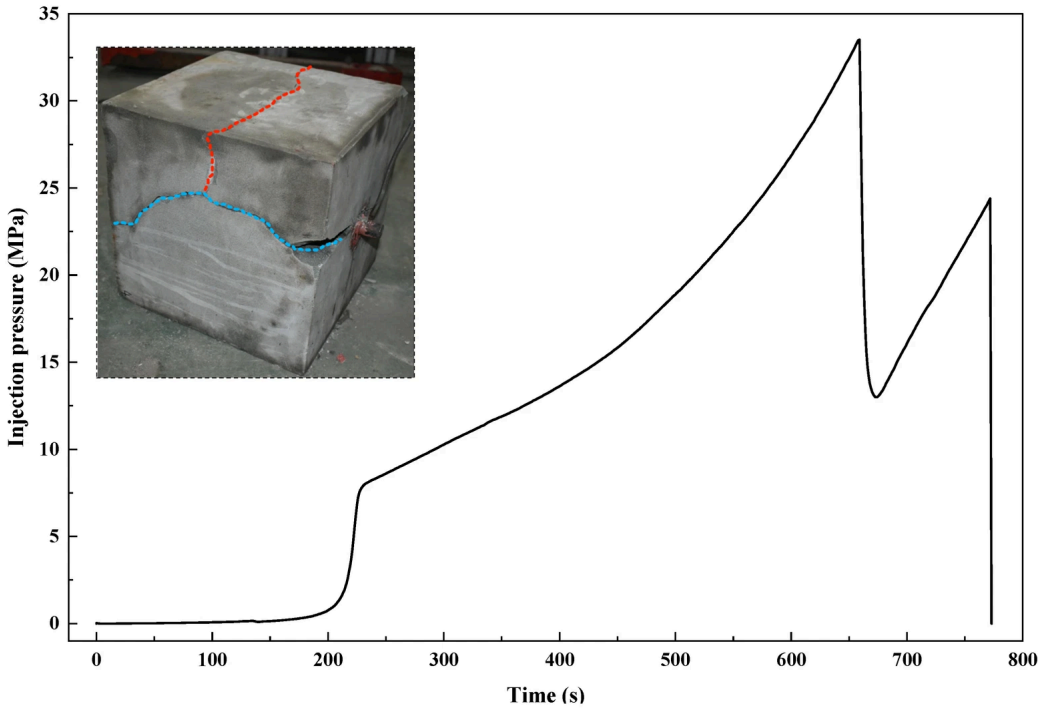


Figure 14. Injection pressure response during true-triaxial fracturing. Inset: post-fracturing specimen showing the generated fracture morphology.

As shown in Figure 14, the injection pressure remained nearly constant during the initial stage of injection. After approximately 220 s, the pressure rapidly increased to about 8 MPa and then continued to rise steadily, reaching a maximum value of approximately 33.5 MPa at around 660 s. Subsequently, a pronounced pressure drop occurred, with the pressure decreasing from 33.5 MPa to approximately 13 MPa, indicating fracture initiation and rapid fracture propagation within the specimen. Notably, after the first pressure drop, the pressure did not continue to decrease but gradually increased again to approximately 24 MPa, followed by a second distinct pressure drop at around 770 s. The subsequent pressure build-up and release behavior indicates that fracture propagation continued after the initial breakdown event and that the injected fluid continued to drive further fracture extension.

The inset in Figure 14 shows the post-fracturing specimen. Two visible fractures originating from the vicinity of the borehole were observed, extending toward different free surfaces of the specimen. One fracture propagated through the side surface of the specimen, whereas the other exhibited a noticeable deviation during propagation and eventually reached the top surface. The presence of multiple fracture paths is consistent with the staged fracture-propagation process reflected by the two pronounced pressure-drop events. These observations indicate that fracture growth was not restricted to a single propagation pathway and resulted in a relatively complex fracture geometry under true-triaxial stress conditions.

Combining the pressure response and fracture morphology results, it can be concluded that the HPG–CO_2 mixed-phase fracturing fluid was capable of initiating and propagating fractures under true-triaxial stress conditions. The formation of multiple fracture paths demonstrates the ability of the system to generate non-planar fracture geometries, providing favorable conditions for increasing the stimulated reservoir volume in unconventional gas reservoirs. These results further verify that the HPG–CO_2 mixed-phase fracturing fluid has potential applicability in CO_2-based gas-reservoir stimulation. For field application, the salinity of the mixing water also needs to be considered. Dissolved ions can affect HPG hydration and borate-crosslinked gel rheology, with Ca^{2+} and Fe^{3+} reported to have more pronounced adverse effects than common monovalent ions [32]. Since deionized water was used in this study, the effects of saline or recycled water on CO_2 dispersion, fluid-loss control, and proppant suspension warrant further investigation.

3. Conclusions

(1) A functional HPG aqueous gel–CO_2 mixed-phase system was constructed using a borate-crosslinked HPG gel as the continuous, structure-forming phase. Fluid-loss tests were used to screen the CO_2 fraction, and the 30%, 40%, and 50% formulations were further evaluated by proppant-settling tests. The 30% formulation exhibited the lowest cumulative fluid loss, whereas the 40% formulation showed the lowest proppant-settling velocity and was therefore selected for subsequent characterization based on both performance criteria.

(2) High-temperature and high-pressure visualization demonstrated that the selected 40% CO_2 HPG gel–CO_2 mixed-phase system maintained stable dispersed structures under all investigated conditions of 20–80 °C and 10–20 MPa. Pressure promoted CO_2 dispersion and bubble refinement, whereas temperature produced a non-monotonic influence on bubble characteristics. In particular, the bubble number reached a minimum and the average bubble diameter increased near 40 °C, indicating a distinct structural transition of the gel-based mixed phase within this temperature range.

(3) Rheological and flow-resistance measurements showed that the crosslinked HPG gel–CO_2 fluid exhibited favorable shear-thinning behavior and stable flow performance over a wide range of temperature and pressure conditions. The rheological response and flow resistance showed a distinct anomaly near 40 °C, consistent with the variation in bubble number and size. This correspondence indicates that macroscopic flow performance arises from coupling between the HPG gel network and the evolving dispersed phase rather than from continuous-phase viscosity alone.

(4) Comparison with the previously reported AM/AA–CO_2 visualization, together with surface-tension and rheological measurements conducted in the present study, demonstrated that the crosslinked HPG gel and AM/AA solution produced fundamentally different structures after contact with CO_2. Although the systems showed comparable surface-tension values and the AM/AA copolymer possessed measurable elasticity, only the HPG gel-based system formed stable dispersed structures. Surface-tension reduction and bulk viscoelasticity are therefore insufficient by themselves to explain mixed-phase formation.

(5) Molecular simulations revealed pronounced interfacial enrichment of HPG chains, whereas the AM/AA copolymer remained predominantly within the aqueous phase. Combined with the component-removal and viscoelasticity results, these findings indicate that HPG-specific interfacial behavior contributes to mixed-phase formation, while the borate-crosslinked HPG gel network provides additional bulk

viscoelastic support for the dispersed structure. True-triaxial experiments further verified the practical performance of the gel-based fluid, with fracture initiation at 33.5 MPa and multiple fracture paths. This gel structure–property–function relationship provides a basis for applying crosslinked polysaccharide gels in CO_2-rich mixed-phase reservoir stimulation.

4. Materials and Methods

4.1. Materials

Industrial-grade hydroxypropyl guar (HPG, grade CJ2-6), industrial-grade organic borate crosslinker (grade JL-9), sodium hydroxide (NaOH), and an acrylamide/acrylic acid (AM/AA) copolymer (grade ZXC; AM:AA molar ratio = 7:3) were supplied by Xi'an Changqing Chemical Group Co., Ltd. (Xi'an, China). Carbon dioxide (purity ≥ 99.9%) was purchased from Wuhan Xinxing Gas Co., Ltd. (Wuhan, China). Quartz sand (100–120 mesh) was used in the proppant-settling experiments. Deionized water was used throughout the study. The HPG was used as received without further purification.

The HPG was further characterized in terms of molar-mass distribution, molar substitution, monosaccharide composition, total carbohydrate content, moisture, and ash. The physicochemical characteristics of the HPG sample are summarized in Table 4, and the corresponding characterization procedures, spectra, chromatograms, and calculation details are provided in the Supplementary Materials.

Table 4. Physicochemical characteristics of the commercial hydroxypropyl guar used in this study.

Characteristic	Result
Total carbohydrate content	56.4 wt%
Moisture	11.73 wt%
Ash	4.79 wt%
Mannose	61.58 mol%
Galactose	33.63 mol%
Mannose + galactose	95.21 mol%
Mannose/galactose ratio	1.83
Molar substitution (MS)	≈0.47
Number-average molar mass, Mn	1.22×10^6 Da
Weight-average molar mass, Mw	1.57×10^6 Da
Dispersity, Đ	1.28

Total carbohydrate content was determined by the phenol–sulfuric acid method using a mannose/galactose mixed standard with a molar ratio of 1.83:1. MS was estimated from the ^{1}H NMR spectrum.

4.2. Apparatus

A self-developed supercritical CO_2 displacement system equipped with a visualized stirring vessel was used for fluid preparation, phase characterization, fluid-loss evaluation, and proppant-settling tests. Rheological properties and dynamic viscoelastic behavior were measured using a HAAKE MARS 60 rheometer (Thermo Fisher Scientific, Dreieich, Germany). Surface tension was determined using a JK99FM automatic tensiometer. Flow resistance performance was evaluated using a self-developed high-temperature and high-pressure long-pipe friction testing system. Fracturing experiments were conducted using a self-developed true-triaxial hydraulic fracturing apparatus.

The overall experimental workflow and characterization strategy adopted in this study are illustrated in Figure 15. Detailed experimental procedures are described in the following sections.

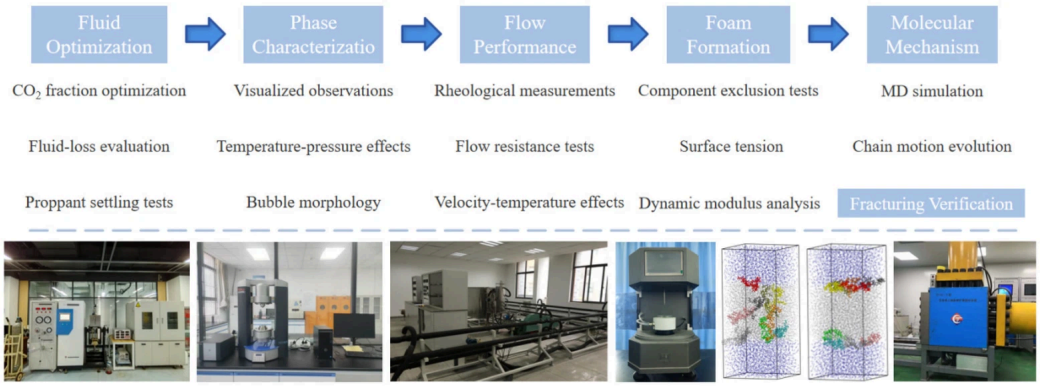


Figure 15. Experimental workflow and characterization strategy adopted in this study.

4.3. Preparation of the Crosslinked HPG Aqueous Gel and HPG Gel–CO_2 Mixed-Phase Fluid

A crosslinked HPG aqueous gel was prepared by hydrating 0.4 wt% HPG in deionized water at 500 rpm for 30 min, followed by the addition of 0.6 wt% organic borate crosslinker and 0.6 wt% NaOH. Under alkaline conditions, borate crosslinking produced a three-dimensional HPG gel network. The mixture was manually stirred for 2 min to obtain a homogeneous aqueous gel.

The HPG gel–CO_2 mixed-phase fracturing fluid was prepared in a visualized high-pressure stirring vessel. A predetermined volume of the crosslinked HPG aqueous gel, used as the continuous gel phase, and CO_2 was introduced into the vessel and mixed at 3000 rpm for 10 min. The nominal CO_2 volume fraction was defined based on the fixed internal volume of the vessel and the initial volume of the aqueous gel. For example, a 40% CO_2 formulation was prepared by filling 60% of the vessel volume with aqueous gel, introducing CO_2 into the remaining space, and bringing the system to the specified temperature and pressure.

4.4. CO_2 Volume Fraction Optimization

4.4.1. Fluid-Loss Test

Fluid-loss tests were conducted to preliminarily evaluate the suitability of different CO_2 volume fractions. The experiments were performed using the supercritical CO_2 displacement system at 40 °C with an inlet pressure of 13.5 MPa and a back pressure of 10 MPa. Artificial sandstone cores with a diameter of 2.5 cm, a length of 5 cm, a gas permeability of approximately 5 mD, and a porosity of approximately 10% were used. Mixed-phase fluids containing CO_2 volume fractions of 10%, 30%, 40%, 50%, and 70% were investigated. Because the volumes of water and CO_2 produced within each 1-min interval were too small to be measured accurately by direct volume readings, water droplets and CO_2 bubbles were counted at 1-min intervals. The average volume per droplet or bubble was determined from the collected volume and corresponding total count during each calibration period, and the minute-by-minute produced volumes were calculated accordingly. The CO_2 volume measured at atmospheric pressure and 40 °C was converted to its equivalent volume at 11.75 MPa and 40 °C using the CO_2 density ratio. The cumulative total produced volume was calculated as the sum of the cumulative water volume and converted CO_2 volume.

4.4.2. Proppant-Settling Test

Based on the preliminary fluid-loss evaluation, several CO_2 volume fractions with promising fluid-loss performance were selected for further proppant-settling tests. The experiments were conducted in the visualized stirring vessel at 10 MPa. Quartz sand

(100–120 mesh) was used as the test particles. The settling behavior was evaluated at 20, 40, 50, 60, 70, and 80 °C. For each condition, three repeated measurements were performed using the same prepared sample. The settling velocity was calculated from the vertical settling distance of a particle over a 10 s observation period. The 10 s observation period was selected to obtain a sufficiently long settling trajectory while allowing continuous tracking of the same particle within the observation window. Measurements were conducted under quiescent conditions, as continuous stirring could move particles out of the visible region and prevent reliable trajectory tracking.

4.5. Phase Characterization

Phase characterization of the HPG–CO_2 mixed-phase fracturing fluid was conducted using the visualized high-pressure stirring vessel. The fluid prepared with the selected CO_2 volume fraction was investigated at temperatures of 20, 40, 60, and 80 °C and pressures of 10 and 20 MPa. After mixing at 3000 rpm for 10 min, images were acquired through the observation window.

For each temperature–pressure condition, images were captured from the upper, middle, and lower sections of the observation window. A central region of 6.5 mm × 13 mm was extracted from each image and analyzed using FIJI software (ImageJ 1.54p). Bubble number and average bubble diameter were determined through image segmentation and particle analysis. The FIJI macro used for image analysis is provided in Supplementary Code S1.

4.6. Rheological Characterization of the HPG Gel–CO_2 Mixed-Phase System

The rheological properties of the HPG–CO_2 mixed-phase fracturing fluid were measured using a HAAKE MARS 60 high-pressure rheometer. Rheological tests were conducted at temperatures ranging from 20 to 80 °C and pressures ranging from 7 to 25 MPa. The shear rate was increased stepwise from 1 to 1000 s^{-1} while maintaining constant temperature and pressure.

Each shear-rate condition was maintained for 10 min to ensure rheological stabilization. The apparent viscosity at a given temperature, pressure, and shear rate was determined by averaging the stable data points with a viscosity fluctuation of less than 0.1 mPa·s.

4.7. Flow Resistance Characterization

The flow resistance characteristics of the HPG–CO_2 mixed-phase fracturing fluid prepared with the selected CO_2 volume fraction were evaluated using the laboratory-built high-temperature high-pressure flow-resistance testing system. Experiments were conducted at temperatures ranging from 20 to 80 °C and a pressure of 10 MPa. Flow velocities of 0.5, 1.0, 1.5, 2.0, and 2.5 m/s were investigated.

After the flow conditions reached a stable state, the pressure drop across a 1 m test section with an inner diameter of 6 mm was recorded. The friction factor was calculated according to:

$$f = \frac{2d}{\rho u^2 L} \Delta P$$

where f is the friction factor, d is the inner diameter of the test section, ρ is the fluid density, u is the average flow velocity, L is the test-section length, and ΔP is the measured pressure drop.

https://doi.org/10.3390/gels12111003

4.8. Interfacial and Viscoelastic Characterization of the Gel Formulations

The interfacial activity and dynamic viscoelasticity of the crosslinked HPG gel and related component-removal formulations were evaluated to determine how gel composition and bulk gel response contribute to mixed-phase formation. In addition, a 0.35 wt% AM/AA copolymer solution (AM:AA molar ratio = 7:3) was used as a comparison polymer fluid. The solution was prepared by slowly adding the AM/AA copolymer to deionized water under continuous stirring until homogeneous. Its surface tension and rheological properties were measured in the present study. The representative AM/AA–CO_2 visualization images in Supplementary Figure S15 were obtained from the previously published study by Chen et al. [29]. Both studies were conducted within the same research program using the same high-pressure visualization apparatus and comparable experimental conditions, including temperatures of 20–80 °C and pressures of 10 and 20 MPa. These previously acquired images were used for qualitative comparison with the HPG–CO_2 system.

Surface tension measurements were performed at ambient conditions using a JK99FM automatic tensiometer based on the Du Noüy ring method. Each sample was measured three times.

Dynamic viscoelastic properties were determined using the HAAKE MARS 60 rheometer. Frequency sweep tests were conducted over a frequency range of 0.1–10 Hz within the linear viscoelastic region. The storage modulus (G′) and loss modulus (G″) were recorded to characterize the viscoelastic behavior and structural strength of the fluids.

4.9. Molecular Dynamics Simulation

To elucidate the interfacial adsorption behavior and structural evolution of polymers at the CO_2–water interface, molecular dynamics (MD) simulations were performed using GROMACS 2025.4 [33]. To investigate the interfacial behavior of the base polymers without the complexity introduced by borate crosslinking, simplified non-crosslinked HPG and AM/AA copolymer models were constructed based on their representative molecular structures (Supplementary Figures S5–S6). For the AM/AA copolymer, the molar ratio of acrylamide to acrylic acid was set to 7:3. To ensure comparable molecular dimensions, the degree of polymerization was set to 4 for HPG and 8 for the AM/AA copolymer, respectively. Ten polymer chains were included in each simulation system. The GAFF2 force field was employed for polymer and CO_2 molecules [34], while water molecules were described using the OPC3 water model. System visualization and trajectory rendering were performed using VMD 1.9.3 [35].

A three-phase simulation box consisting of a central aqueous layer and two CO_2 layers was constructed. The initial box dimensions were approximately 6 × 6 × 12 nm^3. Periodic boundary conditions were applied in all directions. For the HPG system, the aqueous phase contained 6059 water molecules and 10 HPG chains, while 3456 CO_2 molecules were distributed in the upper and lower CO_2 phases. For the AM/AA copolymer system, 6464 water molecules, 10 AM/AA copolymer chains, and 3456 CO_2 molecules were employed. The simulations were conducted under NPT conditions at 313.15 K (40 °C) and 10 MPa using the V-rescale thermostat [36] and C-rescale barostat [37]. After energy minimization and equilibration, a 100 ns production simulation was carried out.

The interfacial behavior of the polymers was analyzed through trajectory snapshots, z-axis number density distributions, interaction energies between polymers and surrounding fluid phases, radius of gyration (Rg), solvent-accessible surface area (SASA), and root-mean-square deviation (RMSD). These analyses were used to characterize poly-

mer migration, conformational evolution, intermolecular interactions, and interfacial adsorption behavior at the CO_2–water interface.

4.10. True-Triaxial Fracturing Experiment

True-triaxial fracturing experiments were conducted to evaluate the fracturing performance of the selected 40% CO_2 HPG–CO_2 mixed-phase fracturing fluid. Cubic artificial sandstone specimens (300 mm × 300 mm × 300 mm) with a gas permeability of approximately 0.5 mD were used. A borehole (25 mm in diameter and 150 mm in depth) was drilled and sealed with a steel injection tube.

The specimen was subjected to principal stresses of σ_v = 15 MPa, σ_H = 15 MPa, and σ_h = 10 MPa using a self-developed true triaxial fracturing apparatus, with the injection direction aligned with the minimum horizontal principal stress. The selected 40% CO_2 HPG–CO_2 mixed-phase fracturing fluid was injected at a constant rate of 60 mL·min^{-1}. Injection pressure was continuously recorded during the experiment. After fracturing, the specimen was removed from the chamber and photographed to characterize the fracture morphology.

4.11. Data Processing and Statistical Analysis

Unless otherwise stated, each experimental condition was evaluated in a single experimental run, without independent sample-preparation replicates. Results from these tests are therefore presented descriptively, without inferential statistical analysis.

For fluid-loss measurements, the cumulative total produced volume at time t was calculated as

$$V_{tot}(t) = V_{water}(t) + V_{CO2,ref}(t)$$

where $V_{water}(t)$ is the cumulative produced water volume and $V_{CO2,ref}(t)$ is the cumulative CO_2 volume converted to 11.75 MPa and 40 °C. The average fluid-loss rates over 0–60 min and 50–60 min were calculated as

$$\bar{q}_{0-60} = \frac{V_{tot}(60)}{60}$$

$$\bar{q}_{50-60} = \frac{V_{tot}(60) - V_{tot}(50)}{10}$$

where the fluid-loss rates are expressed in mL/min.

For proppant-settling tests, the settling velocity was calculated by dividing the vertical settling distance by the 10 s observation period. Three repeated measurements were conducted using the same prepared sample. The results are reported as mean ± standard deviation (SD), with the SD calculated from the three measurements.

Surface-tension results are also reported as mean ± SD based on three measurements per sample. These repeated measurements do not represent independent sample-preparation replicates. For experiments conducted only once per condition, replicate-based uncertainty and statistical significance could not be determined.

Supplementary Materials: The following supporting information can be downloaded at: https://www.mdpi.com/article/10.3390/gels12111003/s1.

Author Contributions: Conceptualization, G.L. and M.F.; methodology, G.L. and T.C.; validation, Y.Z.; formal analysis, G.L.; investigation, G.L., T.C. and Y.Z.; data curation, G.L. and Y.Z.; writing—original draft preparation, G.L.; writing—review and editing, G.L., M.F. and T.C.; visualization, G.L.; supervision, M.F.; project administration, M.F.; funding acquisition, M.F. All authors have read and agreed to the published version of the manuscript.

Funding: This research was funded by Xi'an Changqing Chemical Group Co., Ltd under Contract No. CQJ-HGJT-2025-CL-584.

Institutional Review Board Statement: Not applicable.

Informed Consent Statement: Not applicable.

Data Availability Statement: The original contributions presented in this study are included in the article and Supplementary Materials. The raw data supporting the conclusions of this article will be made available by the corresponding author on reasonable request. During the preparation of this manuscript, the authors used ChatGPT (OpenAI, GPT-5.6, accessed September 2026) for language editing and content organization. The authors reviewed and edited the output and take full responsibility for the content of this publication.

Conflicts of Interest: Tengfei Chen is employed by Xi'an Changqing Chemical Group Co., Ltd., which funded the study and supplied research materials. Tengfei Chen contributed to methodology, investigation, and writing—review and editing. The sponsor's involvement was limited to the disclosed funding and material support and the disclosed co-author contributions. The remaining authors declare no conflicts of interest.

References

1. Gao, J.; Wang, H.; Sharma, M. Research progress and prospects of CO_2 fracturing for developing unconventional energy sources. *Geoenergy Sci. Eng.* **2024**, *241*, 213137. [Google Scholar] [CrossRef]
2. Han, L.; Shi, X.; Ni, H.; Zhang, W.; Gao, Q. Review of CO_2 fracturing and carbon storage in shale reservoirs. *Energy Fuels* **2024**, *38*, 15913–15934. [Google Scholar] [CrossRef]
3. Zhang, X.; Zhang, S.; Zou, Y.; Li, N.; Li, J.; Shi, L. Fracture propagation characteristics of water and CO_2 fracturing in continental shale reservoirs. *Phys. Fluids* **2024**, *36*, 106614. [Google Scholar] [CrossRef]
4. Hazarika, S.; Boruah, A. Supercritical CO_2 (SCO_2) as alternative to water for shale reservoir fracturing. *Mater. Today Proc.* **2022**, *50*, 1754–1757. [Google Scholar] [CrossRef]
5. Shi, W.; Zhu, L.; Guo, M.; Huang, Z.; Wang, G.; Lin, L.; He, L.; Liao, Y.; He, H.; Gong, J. Assessment of CO_2 fracturing in China's shale oil reservoir: Fracturing effectiveness and carbon storage potential. *Resour. Conserv. Recycl.* **2023**, *197*, 107101. [Google Scholar] [CrossRef]
6. Yang, B.; Wang, H.Z.; Li, G.S.; Wang, B.; Chang, L.; Tian, G.H.; Zhao, C.M.; Zheng, Y. Fundamental study and utilization on supercritical CO_2 fracturing developing unconventional resources: Current status, challenge and future perspectives. *Pet. Sci.* **2022**, *19*, 2757–2780. [Google Scholar] [CrossRef]
7. Meng, S.; Zhang, F.; Tao, J.; Jin, X.; Xu, J.; Liu, H. Carbon storage potential of shale reservoirs based on CO_2 fracturing technology. *Engineering* **2025**, *48*, 121–127. [Google Scholar] [CrossRef]
8. Wang, X.Z.; Guo, X.; Sun, X. Basic research and technological progress of CO_2 fracturing. *Pet. Sci. Bull.* **2024**, *9*, 931–943. (In Chinese) [Google Scholar] [CrossRef]
9. Zhou, X.M.; Li, L.; Sun, Y.Q.; Liu, R.; Guo, Y.C.; Hao, Y.M.; Su, Y.L. Investigation of influence factors on CO_2 flowback characteristics and optimization of flowback parameters during CO_2 dry fracturing in tight gas reservoirs. *Pet. Sci.* **2023**, *20*, 3553–3566. [Google Scholar] [CrossRef]
10. Qiao, D.; Wang, X.; Meng, L.; Chen, J.; Yu, J.; Chi, Q.; Li, S. Research status and prospect of liquid carbon dioxide fracturing technology. *Sci. Soc. Res.* **2024**, *6*, 179–184. [Google Scholar] [CrossRef]
11. Yang, J.; Lian, H.; Li, L. Fracturing in coals with different fluids: An experimental comparison between water, liquid CO_2, and supercritical CO_2. *Sci. Rep.* **2020**, *10*, 18681. [Google Scholar] [CrossRef]

12. Zhang, X.; Lu, Y.; Tang, J.; Zhou, Z.; Liao, Y. Experimental study on fracture initiation and propagation in shale using supercritical carbon dioxide fracturing. *Fuel* **2017**, *190*, 370–378. [Google Scholar] [CrossRef]
13. Zhou, D.; Zhang, G.; Wang, Y.; Xing, Y. Experimental investigation on fracture propagation modes in supercritical carbon dioxide fracturing using acoustic emission monitoring. *Int. J. Rock Mech. Min. Sci.* **2018**, *110*, 111–119. [Google Scholar] [CrossRef]
14. Denney, D. Fluid selection for energized hydraulic fractures. *J. Pet. Technol.* **2010**, *62*, 42–44. [Google Scholar] [CrossRef]
15. Faroughi, S.A.; Pruvot, A.J.C.J.; McAndrew, J. The rheological behavior of energized fluids and foams with application to hydraulic fracturing: A review. *J. Pet. Sci. Eng.* **2018**, *163*, 243–263. [Google Scholar] [CrossRef]
16. Liu, G.; Bai, X.D.; Ma, Z.G.; Zheng, Y.; Yang, H.; Zhang, M. Research and application of atmospheric-pressure sand-mixing near-dry fracturing technology. *Drill. Fluid Complet. Fluid* **2021**, *38*, 375–379. (In Chinese) [Google Scholar] [CrossRef]
17. Lin, S.; Chang, X.; Yang, C.; Guo, Y.; Shi, X. Integrated supercritical CO_2 injection for shale reservoir enhancement: Mechanisms, experimental insights, and implications for energy and carbon storage. *Energy* **2025**, *324*, 135908. [Google Scholar] [CrossRef]
18. Hou, L.; Luo, J.; Gong, P.; Ji, Y.; Zhang, L. Promotion of CO_2 fracturing for CCUS—The technical gap between theory and practice. *Front. Energy Res.* **2024**, *12*, 1348375. [Google Scholar] [CrossRef]
19. Wang, S.; Tang, H.; Guo, J.; Wang, K. Effect of pH on the rheological properties of borate crosslinked hydroxypropyl guar gum hydrogel and hydroxypropyl guar gum. *Carbohydr. Polym.* **2016**, *147*, 455–463. [Google Scholar] [CrossRef]
20. Qiu, L.; Shen, Y.; Wang, T.; Wang, C. Rheological and fracturing characteristics of a novel sulfonated hydroxypropyl guar gum. *Int. J. Biol. Macromol.* **2018**, *117*, 974–982. [Google Scholar] [CrossRef]
21. Thombare, N.; Jha, U.; Mishra, S.; Siddiqui, M.Z. Guar gum as a promising starting material for diverse applications: A review. *Int. J. Biol. Macromol.* **2016**, *88*, 361–372. [Google Scholar] [CrossRef]
22. Yi, Y.; Wu, L.; Zhang, J.; Wang, H.; Xie, X.; Gang, C. Sulfonation modification of guar gum and its performance as a fracturing fluids thickener. *Pol. J. Chem. Technol.* **2024**, *26*, 29–38. [Google Scholar] [CrossRef]
23. Meng, L.; Li, S.S.; Liu, L.F.; Wang, L.L.; Zu, K.; Xie, G.Q. Development and performance evaluation of a guar gum fracturing fluid system resistant to 155 °C. *Drill. Prod. Technol.* **2022**, *45*, 133–138. (In Chinese) [Google Scholar]
24. Zhang, C.; Wang, Y.; Wang, Z.; Wang, H.; Liang, S.; Xu, N.; Li, D. Mechanism analysis of enhancing the temperature and shear resistance of hydroxypropyl guar gum fracturing fluid by boron-functionalized nanosilica colloidal crosslinker. *Colloids Surf. A Physicochem. Eng. Asp.* **2023**, *676*, 132154. [Google Scholar] [CrossRef]
25. Zhou, C.; Chen, Y.; Xiao, Y.; Wu, Y.; Yang, C.; Yu, M.; Liu, L. Preparation and performance analysis of nano-crosslinking agent for sulphonated guar gum fracturing fluid. *Can. J. Chem. Eng.* **2025**, *103*, 953–963. [Google Scholar] [CrossRef]
26. Gao, Y.; Wang, M.; Zhang, H.; Wu, D.; Gao, F. Performance optimization and damage control of ultralow-concentration guar gum fracturing fluids for tight sandstone reservoirs. In Proceedings of the 2025 IEEE 2nd International Conference on Energy and Electrical Engineering (EEE), Nanchang, China, 20–21 June 2025; pp. 432–435. [Google Scholar] [CrossRef]
27. Li, Q.; Wang, F.; Wang, Y.; Forson, K.; Cao, L.; Zhang, C.; Zhou, C.; Zhao, B.; Chen, J. Experimental investigation on the high-pressure sand suspension and adsorption capacity of guar gum fracturing fluid in low-permeability shale reservoirs: Factor analysis and mechanism disclosure. *Environ. Sci. Pollut. Res.* **2022**, *29*, 53050–53062. [Google Scholar] [CrossRef]
28. Wang, J.; Zhou, F.; Bai, H.; Wei, D.; Ma, J.; Yang, P.; Zhang, F.; Yuan, L. A new approach to study the friction-reduction characteristics of viscous/conventional slickwater in simulated pipelines and fractures. *J. Nat. Gas. Sci. Eng.* **2020**, *83*, 103620. [Google Scholar] [CrossRef]
29. Chen, T.; Zhou, S.; Yao, T.; Fu, M.; Wen, Z.; Shen, Q. Performance of a high-molecular-weight AM/AA copolymer in a CO_2–water polymer hybrid fracturing fluid under high-temperature and high-pressure conditions. *Polymers* **2026**, *18*, 418. [Google Scholar] [CrossRef]
30. Li, G.; Fu, M.; Hu, J.; Lu, S.; Meng, F. Study of thickened CO_2 flooding for enhancing oil recovery in low-permeability sandstone reservoirs. *Fuel* **2025**, *385*, 134148. [Google Scholar] [CrossRef]
31. Zhao, J.; Yu, Y.; Wu, K.; Liu, Y.; Zhu, Y.; Lu, H.; Yue, H.; Liang, B. A novel CO_2 foam stabilizer based on natural polysaccharide psyllium seed gum: Experimental and molecular dynamics analysis. *Carbohydr. Polym.* **2025**, *367*, 123972. [Google Scholar] [CrossRef]
32. Liu, B.; Li, Z.; Wang, L.; Li, C.; Wu, Y.; Li, Y.; Zhao, D.; Chen, G.; Bi, W. Impact of mono-, di-, and trivalent ions on the rheology of borate-crosslinked guar fracturing fluids. *Gels* **2026**, *12*, 373. [Google Scholar] [CrossRef]

33. Abraham, M.J.; Murtola, T.; Schulz, R.; Páll, S.; Smith, J.C.; Hess, B.; Lindahl, E. GROMACS: High performance molecular simulations through multi-level parallelism from laptops to supercomputers. *SoftwareX* **2015**, *1–2*, 19–25. [Google Scholar] [CrossRef]
34. Wang, J.; Wolf, R.M.; Caldwell, J.W.; Kollman, P.A.; Case, D.A. Development and testing of a general amber force field. *J. Comput. Chem.* **2004**, *25*, 1157–1174. [Google Scholar] [CrossRef]
35. Humphrey, W.; Dalke, A.; Schulten, K. VMD: Visual molecular dynamics. *J. Mol. Graph.* **1996**, *14*, 33–38. [Google Scholar] [CrossRef]
36. Bussi, G.; Donadio, D.; Parrinello, M. Canonical sampling through velocity rescaling. *J. Chem. Phys.* **2007**, *126*, 014101. [Google Scholar] [CrossRef]
37. Bernetti, M.; Bussi, G. Pressure control using stochastic cell rescaling. *J. Chem. Phys.* **2020**, *153*, 114107. [Google Scholar] [CrossRef]

Disclaimer/Publisher's Note: The statements, opinions and data contained in all publications are solely those of the individual author(s) and contributor(s) and not of MDPI and/or the editor(s). MDPI and/or the editor(s) disclaim responsibility for any injury to people or property resulting from any ideas, methods, instructions or products referred to in the content.